RESEARCH ARTICLE

Key Points:
- A revised set of 60 CRISM summary products captures Mars' spectral diversity
- A library of 30 surface type spectra identified using CRISM is presented
- New "browse products" demonstrate surface spectral variability

Revised CRISM spectral parameters and summary products based on the currently detected mineral diversity on Mars

Christina E. Viviano-Beck[1], Frank P. Seelos[1], Scott L. Murchie[1], Eliezer G. Kahn[1], Kimberley D. Seelos[1], Howard W. Taylor[1], Kelly Taylor[2], Bethany L. Ehlmann[3,4], Sandra M. Wiseman[5], John F. Mustard[5], and M. Frank Morgan[1]

[1]Johns Hopkins University Applied Physics Laboratory, Laurel, Maryland, USA, [2]Corning Inc., Corning, New York, USA, [3]Division of Geological and Planetary Sciences, California Institute of Technology, Pasadena, California, USA, [4]Jet Propulsion Laboratory, California Institute of Technology, Pasadena, California, USA, [5]Geological Sciences, Brown University, Providence, Rhode Island, USA

Abstract The investigation of hyperspectral data from the Mars Reconnaissance Orbiter Compact Reconnaissance Imaging Spectrometer for Mars (CRISM) and the Observatoire pour la Minéralogie, L'Eau, les Glaces et l'Activitié (OMEGA) on Mars Express has revealed an increasingly diverse suite of minerals present on the Martian surface. A revised set of 60 spectral parameters derived from corrected spectral reflectance at key wavelengths in CRISM targeted observations and designed to capture the known diversity of surface mineralogy on Mars is presented here as "summary products." Some of the summary products have strong heritage to OMEGA spectral parameter calculations; this paper also presents newly derived parameters that highlight locations with more recently discovered spectral signatures. Type locations for the diversity of currently identified mineral spectral signatures have been compiled into a library presented in this work. Our analysis indicates that the revised set of summary products captures the known spectral diversity of the surface, and successfully highlights and differentiates between locations with differing spectral signatures. The revised spectral parameter calculations and related products provide a useful tool for scientific interpretation and for future mission landing site selection and operations.

1. Introduction

Recent visible to short-wavelength infrared (VSWIR) orbital observations of Mars reveal widespread and diverse minerals present on the surface that record a complex history of changing geologic processes and climatic conditions. Thirty unique VSWIR spectral signatures indicate a wide range of primary and alteration minerals that have been detected in the analyses of data from the Observatoire pour la Mineralogie, l'Eau, les Glaces et l'Activité (OMEGA) [*Bibring et al.*, 2004] instrument on board Mars Express and the Compact Reconnaissance Imaging Spectrometer for Mars (CRISM) [*Murchie et al.*, 2007] instrument on board the Mars Reconnaissance Orbiter (MRO) [*Zurek and Smrekar*, 2007]. Constraining the nature and distribution of both primary and secondary mineralogy on the surface of Mars is central to understanding igneous processes that formed the crust, and subsequent alteration of it by liquid water on the surface or in the subsurface and by impacts and exposure to the low-pressure atmosphere of Mars.

OMEGA and CRISM measure the VSWIR to midinfrared portions of the spectrum (0.35–5.2 μm and 0.362–3.92 μm, respectively). OMEGA began its science phase in 2004 and CRISM in 2006. The OMEGA instrument has a spatial sampling ranging from 350 to 10,000 m/pixel depending on the orbital altitude and a set of 352 bands or 400 bands (sampled at 7.5 nm from 0.35 to 1.05 μm, 14 nm from 0.94 to 2.70 μm, and ~21 nm from 2.65 to 5.2 μm). CRISM can be targeted with a high spatial sampling of 18 or 36 m/pixel, or a survey mode at 100 or 200 m/pixel. CRISM targeted observations have hyperspectral resolution (544 bands, sampled at 6.55 nm), while survey mode spectral resolution can range from 72 to 261 bands depending on the observation mode, with sampling density varying from 53.4 nm between channels at sparsely sampled wavelengths to contiguous sampling at 6.55 nm/channel.

In this paper we summarize the state of knowledge of the VSWIR surface spectral variability and identified mineralogy on the surface of Mars from CRISM after more than 7 years of measurements. We have

assembled 30 type spectra of minerals identified using CRISM data into the Mineral Identified through CRISM Analysis (MICA) Library. These type spectra are derived from published results of numerous investigations of surface mineralogy using CRISM data. Type spectra are used to "tune" existing CRISM spectral summary product definitions [*Pelkey et al.*, 2007], taking advantage of the full hyperspectral sampling of CRISM data, to improve upon and augment the summary products catalog. Meaningful threshold values for the summary products have also been defined for both the CRISM global data set and for individual CRISM observations. We also summarize the display of thematically related summary products as red-green-blue (RGB) color composite "browse products" that allow for rapid assessment of surface spectral variability.

2. CRISM Data: Reduction and Analysis

CRISM data presented in this paper are from new Map-projected Targeted Reduced Data Record (MTRDR) products, derived by processing CRISM hyperspectral targeted observations recording radiance at sensor through a series of standard spectral corrections, spatial transforms, and renderings. A companion paper (F. P. Seelos et al., manuscript in preparation) and preliminary abstract [*Seelos et al.*, 2012] detail the nature of these corrections and demonstrate major advances in the accessibility of CRISM spectral information through the MTRDR product suite. The MTRDR data processing pipeline includes a basic photometric correction for Lambertian scattering, and an updated "volcano scan" atmospheric correction [*Bibring et al.*, 1989; *Langevin et al.*, 2005; *McGuire et al.*, 2009] that accommodates subtle shifts in the instrument wavelength calibration [*Morgan et al.*, 2011]. Additionally, empirical corrections are applied to remove spectral smile (cross-track shift in wavelength calibration) and mitigate data characteristics related to the continuously varying observation geometry and atmospheric path length [*Murchie et al.*, 2007] inherent to CRISM hyperspectral targeted (gimbaled) observations [*Seelos et al.*, 2011]. Data from the visible/near-infrared (VNIR) detector (0.4–1.0 μm) are transformed to align with the infrared (IR) detector (1.0–3.9 μm), creating a VNIR-IR full spectral range (joined) image cube. The transformation is applied by identifying the closest VNIR pixel to an IR pixel (based on geographic coordinates) and joining its spectrum to the IR spectrum via nearest neighbor resampling, chosen to avoid spectral averaging. The full MTRDR pipeline is applied to all CRISM data presented here, prior to the production of summary products or browse products. Lastly, due to a nonlinear decrease in the spectral response approaching the longest wavelengths of the VNIR detector, small variable offsets remain in extracted unratioed MTRDR spectra at the join between the VNIR and IR detectors. We quantitatively determined the offset between overlapping wavelengths in the VNIR and IR detectors and used a fourth-order polynomial with an onset at ~720 nm to multiplicatively adjust the VNIR reflectance until it matched the IR via nonlinear least squares fitting. This correction was applied to all MICA library spectra. Public release of documented MTRDRs is planned for late 2014.

3. The MICA Library

The original CRISM summary products were specifically designed for the CRISM 72-band multispectral mapping mode wavelength selection, based on a priori knowledge of surface composition from OMEGA data [*Pelkey et al.*, 2007]. Over 7 years have passed since then, during which continued OMEGA and high spatial resolution CRISM hyperspectral imagery have been used to detect a growing number of spectrally diverse minerals on the surface. Thus, it is timely for the summary products to be formally expanded to reflect the complete spectral diversity of the surface recognized in the CRISM/OMEGA wavelength range. We present a brief overview of the type locations of the spectra that make up the MICA library below to provide context for the changes and additions to the revised summary products. Several recent synthesis papers [*Murchie et al.*, 2009; *Carter et al.*, 2013b; *Ehlmann and Edwards*, 2014] and references therein provide global and morphologic context for the majority of the MICA type spectra. The source for each type spectra is detailed in Table 1, reporting the CRISM observation ID and precise location for the most representative example of each MICA type spectra. The details of this table correspond to the ratioed spectra presented in Figures 1–6. Furthermore, the MICA spectral library is being made available at the CRISM website (http://crism.jhuapl.edu/) and archived at the Planetary Data System (PDS) Geosciences Node.

3.1. Ices

Water and CO_2 ices are present on Mars in the form of seasonal frosts in the polar regions, clouds, and part of the large northern and southern permanent polar caps. While both phases may be mixed within a single

Table 1. Location of MICA Type Spectra and Corresponding Library Material[a]

CRISM Phase	Observation ID and Reference[b]	Latitude (N)	Longitude (E)	Numerator Y	Numerator X	Denominator Y	Denominator X	# of Pixels	Laboratory Analog Material
			Ices						
H$_2$O ice	HRL00002885 [*Cull et al.*, 2010][e]	81.817	−170.831	26	412	26	397	7×7	H$_2$O Ice GDS136 (77 K)[c]
CO$_2$ ice	FRT00007E26 [*Brown et al.*, 2010][e]	−84.786	−61.459	333	349	333	257	9×9	CO$_2$ Ice (2 mm)[f]
			Iron Oxides and Primary Mafic Silicates						
Hematite	FRT0000B385 [*Roach et al.*, 2010a]	−13.229	−47.456	366	202	366	304	9×9	Hematite GD327[c]
Mg-Olivine	FRT0000C26C [*Skok et al.*, 2012]	56.803	−9.233	598	365	598	384	5×5	Forsterite LASC02[d]
Fe-Olivine	FRT00003E12 [*Mustard et al.*, 2009]	22.310	77.023	443	401	443	296	9×9	Fayalite LAPO05[d]
Plagioclase	FRT000082EE [*Wray et al.*, 2013]	8.868	67.290	325	76	325	430	9×9	Plagioclase NCLS04[d]
Low-Ca Pyroxene	FRT000064D9 [*Mustard et al.*, 2008]	21.131	74.184	528	174	528	81	9×9	Orthopyroxene LAPP47B[d]
High-Ca Pyroxene	FRT00008F68 [*Skok et al.*, 2010b][d]	20.377	70.129	549	348	549	429	7×7	Pyroxene NBPP22[d]
			Sulfates						
Monohydrated Sulfate	FRT0000A91C [*Roach et al.*, 2009]	−8.579	−79.485	470	178	470	209	11×11	Kieserite F1CC15[d]
Alunite	FRT0000B252 [*Swayze et al.*, 2008]	−30.608	−157.911	99	302	99	260	7×7	Alunite F1CC08B[d]
Hydroxlated Fe-Sulfate	FRT000098B2 [*Lichtenberg et al.*, 2010]	3.897	−20.418	107	137	107	92	5×5	Ferric Hydroxysulfate[g]
Jarosite	FRT00013F5B [*Viviano et al.*, 2013b]	−10.223	−75.451	302	234	302	96	9×9	Jarosite LASF21A[d]
Polyhydrated Sulfate	FRT00009C0A [*Bishop et al.*, 2009]	−4.391	−62.317	396	303	396	279	11×11	Mg Sulfate 799F366[d]
Gypsum	HRL0000CA5C [*Calvin et al.*, 2009][e]	80.372	−116.245	31	58	31	299	11×11	Gypsum LASF41A[d]
Bassanite	FRT00009326 [*Wray et al.*, 2010]	23.008	−18.505	489	385	489	283	7×7	Bassanite GDS145[c]
			Phyllosilicates						
Kaolinite	FRT0000ABCB [*Ehlmann et al.*, 2009]	20.866	73.268	389	222	387	338	5×5	Kaolinite LAKA04[d]
Al-smectite	FRT00003BFB [*Bishop et al.*, 2008]	22.410	−18.221	379	58	379	76	5×5	Montmorillonite LAMO02[d]
Margarite	FRT0000634B [*Carter et al.*, 2013b]	−26.854	−101.244	531	90	531	122	5×5	Margarite GDS106[c]
Illite/Muscovite	FRT0000454E [*Ehlmann et al.*, 2009]	20.194	70.186	103	406	103	373	5×5	Illite LAIL02[d]
Fe-smectite	FRT0000A425 [*Farrand et al.*, 2009]	25.198	−20.172	98	93	98	18	7×7	Nontronite NCJB26[d]
Mg-smectite	FRT00009365 [*Ehlmann et al.*, 2009]	15.780	72.072	198	206	198	126	11×11	Saponite LASA5[d]
Talc	FRT00009D44 [*Viviano et al.*, 2013a]	20.019	73.660	416	84	416	159	5×5	Talc GDS23[c]
Serpentine	FRT0000634B [*Ehlmann et al.*, 2010]	−26.878	−101.180	333	25	333	57	5×5	Serpentine LALZ01[d]
Chlorite	FRT0000A546 [*Michalski and Niles*, 2010]	3.116	57.807	175	269	175	298	11×11	Chlorite LACL14[c]
Prehnite	FRT000050F2 [*Ehlmann et al.*, 2009]	14.997	72.112	381	121	381	264	7×7	Zeolite/Prehnite LAZE03[d]
			Carbonates						
Mg-Carbonate	FRT00003E12 [*Ehlmann et al.*, 2008]	22.213	77.141	136	103	136	211	5×5	Magnesite F1CC06B[d]

Table 1. (continued)

CRISM Phase	Observation ID and Reference[b]	Latitude (N)	Longitude (E)	Numerator		Denominator		# of Pixels	Laboratory Analog Material
				Y	X	Y	X		
Ca/Fe-Carbonate	FRT0000A546 [*Michalski and Niles*, 2010]	3.039	57.737	437	63	437	162	11 × 11	Calcite CAGR01[d]
	Halides and Other Hydrated Silicates								
Hydrated Silica	FRT00009312 [*Ehlmann et al.*, 2009]	19.904	65.918	154	170	154	370	11 × 11	Hydrated Si BKR1JB329C[d]
Epidote	FRT0000CBE5 [*Carter et al.*, 2013a]	17.180	76.405	330	16	330	48	5 × 5	Epidote GDS26[c]
Analcime	FRT00009312 [*Ehlmann et al.*, 2009]	19.982	65.883	243	413	243	399	5 × 5	Analcime GDS1[c]
Chloride	FRT0000AB81 [*Murchie et al.*, 2009]	−31.562	−153.633	413	317	413	116	13 × 13	Halite HS433[c]

[a]Superscripts with the analog materials indicate the origin of those spectra. Numerator and denominator (*x, y*), or (row, column) coordinates are defined for unprojected CRISM cubes.
[b]The references listed refer to the most representative example observation of the phase, not necessarily its first identification.
[c]See *Clark et al.* [1990].
[d]RELAB (http://www.planetary.brown.edu/relab/).
[e]Study of comparable location and mineralogy (exact targeted observation is not directly identified).
[f]See *Hansen* [1997].
[g]See *Lichtenberg et al.* [2010].

CRISM pixel, contributions from the different ices can be discriminated by the broad 1.5 μm absorption feature distinctive of crystalline H_2O ice, and the narrow 1.435 μm absorption (asymmetric stretching overtone) feature in CO_2 ice spectra [*Fink and Sill*, 1982] (Figure 1). This narrow absorption is particularly useful as it does not saturate until large path lengths (>20 cm), is not obscured by atmospheric CO_2 bands at 2 μm, and is 2.3 times stronger than the next strongest minor CO_2 ice bands at 2.281 μm [*Langevin et al.*, 2007]. The strengths of ice absorption features are dependent upon the mean path length of photons within the ice, which is related to the distance between grain boundaries or fractures, and the density of scattering particles (inclusions of dust) within the ice.

3.2. Iron Oxides and Primary Mafic Silicates

Variations in the presence and cation composition of anhydrous minerals are important for understanding the primary mineralogy and geologic evolution of the Martian crust. Constraining the composition and distribution of primary mafic silicates exposed at the surface and excavated from depth can refine petrologic formation models of the crust. Iron oxides are a widespread component of Martian surface soils and dust and highlight the role of recent weathering and surface processes on Mars.
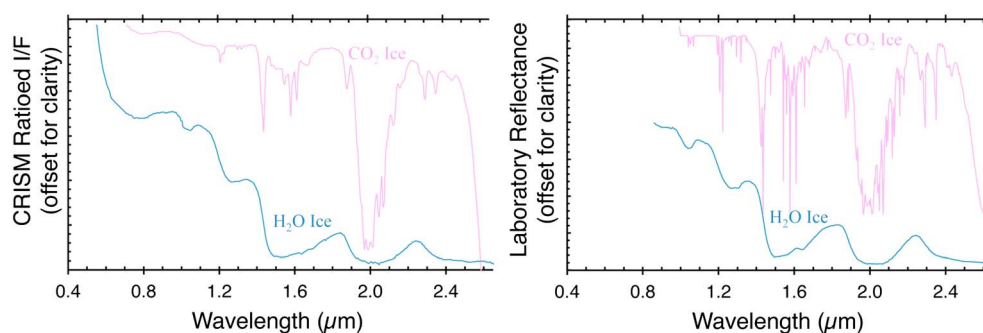

Figure 1. MICA type spectra of (left) ices and (right) laboratory analog materials. Sources for both CRISM and laboratory spectra in Figures 1–6 are given in Table 1. Spectra in Figures 1–6 are generally ordered from bottom to top to emphasize the shift in diagnostic absorption features to longer wavelengths in this wavelength range.
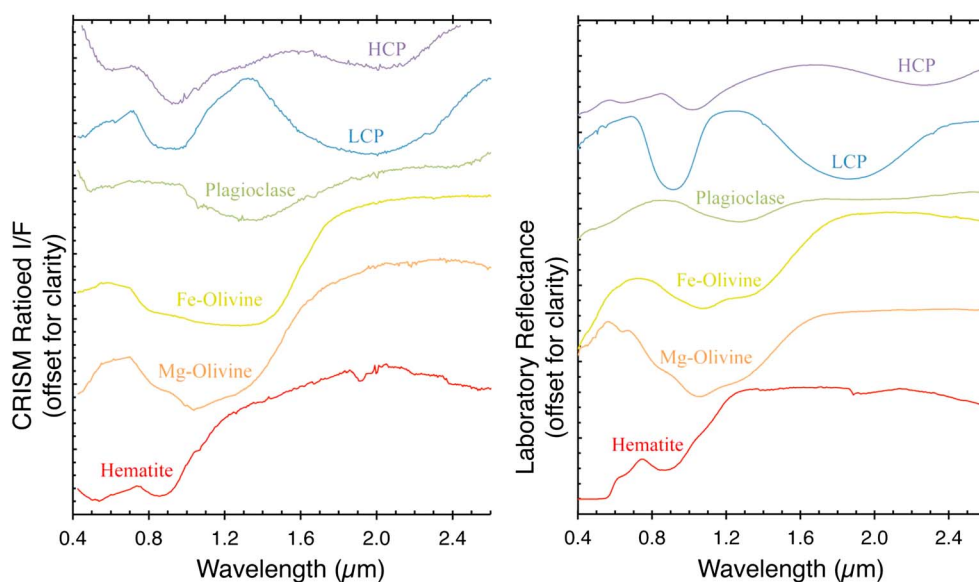
Figure 2. MICA type spectra of (left) iron oxides and primary mafic silicates and (right) laboratory analog materials.

3.2.1. Iron Oxides

Iron oxides have been detected through telescopic, orbital, and in situ observations of the surface of Mars, through the strong ferric absorption edge at 0.53 μm [*Bell et al.*, 1992; *Morris et al.*, 2000; *Farrand et al.*, 2006; *Poulet et al.*, 2007]. Although spectrally this phase is relatively featureless at wavelengths covered by the CRISM IR detector, the VNIR detector covers the 0.4–0.9 μm Fe^{3+} field transitions (e.g., hematite spectrum in Figure 2) and demonstrates the utility of the joined VNIR-IR CRISM image cube in end-member detection. Measuring the bands at 0.53 μm and near 0.9 μm is useful for identifying and discriminating Fe^{3+}-bearing jarosite, maghemite, nanophase oxides, and hematite on Mars [*Morris et al.*, 2000]. The degree of crystallinity of hematite is most clearly indicated by a broad near-infrared absorption centered near 0.86 μm [*Bell et al.*, 2000], near the CRISM detector boundary.

3.2.2. Olivine

Olivine on the surface of Mars shows wide variability in composition, reportedly ranging from Fo_{91} to Fo_5 [*Hoefen et al.*, 2003; *Koeppen and Hamilton*, 2008; *Skok et al.*, 2012]. Olivine has a broad absorption centered near 1 μm that strengthens in depth and broadens with increasing iron content [*King and Ridley*, 1987]. Both an increase in Fe substitution and an increase in grain size will broaden the 1 μm band, such that
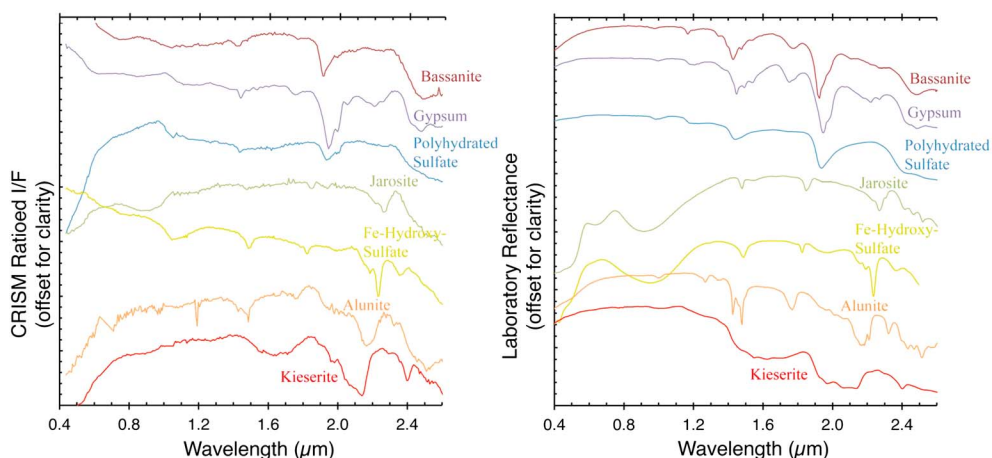
Figure 3. MICA type spectra of (left) sulfates and (right) laboratory analog materials.
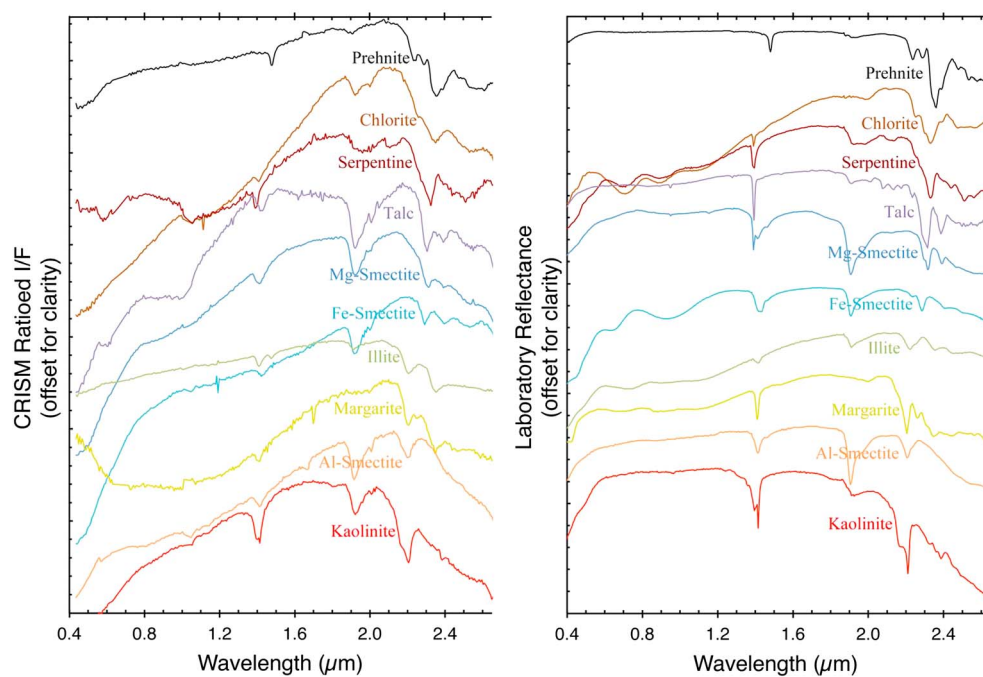
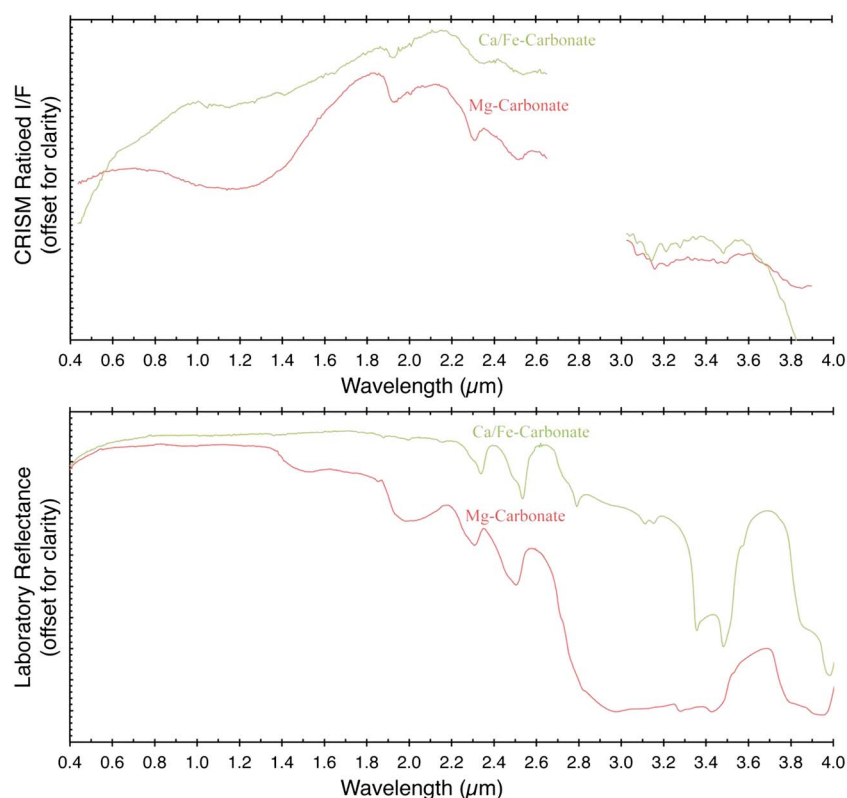**Figure 4.** MICA type spectra of (left) phyllosilicates and (right) laboratory analog materials.

Figure 5. MICA type spectra of (top) carbonates and (bottom) laboratory analog materials.
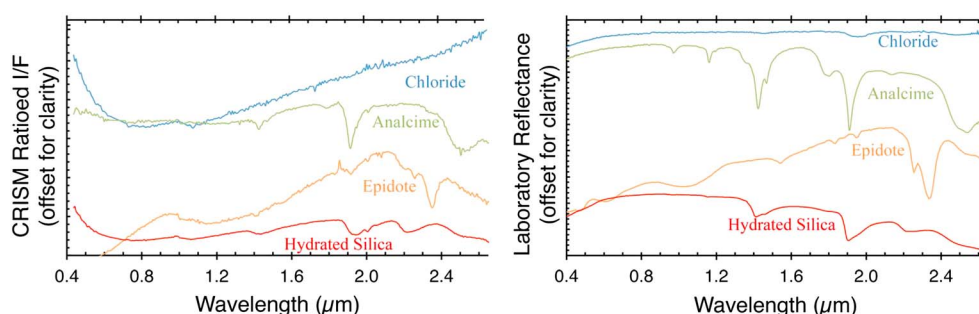
Figure 6. MICA type spectra of (left) halides and other hydrated silicates and (right) laboratory analog materials.

coarse-grained low-iron olivine is spectrally similar to fine-grained high-iron olivine [*Mustard et al.*, 2005]. The 1 μm feature results from electronic transitions from Fe^{2+} in three cation sites within the crystal structure that produce overlapping spectral features and give the appearance of a broad 1 μm band [*Burns*, 1993]. Although the feature extends across the CRISM VNIR-IR detector boundary, longward of 1.5 μm olivine spectra is relatively featureless (Figure 2). Olivine has been detected where Noachian-aged materials are exposed in early Hesperian crater floors and intercrater plains in the southern highlands [*Rogers and Fergason*, 2011], in the basin ring massifs and ejecta of the Argyre, Hellas, and Isidis basins [*Hoefen et al.*, 2003; *Tornabene et al.*, 2008; *Mustard et al.*, 2009; *Bishop et al.*, 2013], in intercrater dunes, ejecta, and deposits in the northern plains where subjacent Noachian rocks have been exposed [*Poulet et al.*, 2007], in sands and bedrock material on the floor of Valles Marineris [*Edwards et al.*, 2008], in isolated blocks surrounding Hellas basin [*Ody et al.*, 2013], and in dikes in several locations including the walls of Valles Marineris [*Flahaut et al.*, 2011], in Thaumasia Planum [*Huang et al.*, 2012], and near the dichotomy boundary [*Pan and Ehlmann*, 2014].

3.2.3. Plagioclase

Plagioclase is the most abundant mineral exposed on the surface of Mars [*Bandfield et al.*, 2000; *Bandfield*, 2002] and also provides information about the magmatic evolution of the crust. Mars Global Surveyor Thermal Emission Spectrometer (TES) [*Christensen et al.*, 2001] indicates the average plagioclase composition is ~ An_{60} with little variability (An_{50}–An_{90}) [*Milam et al.*, 2010]. Recently, several exposures of feldspar-rich materials have been observed in CRISM-targeted observations [*Carter and Poulet*, 2013; *Wray et al.*, 2013]. In mixtures with pyroxene and olivine, feldspar is typically undetectable in the VSWIR range of CRISM due to its spectral blandness. However, minor substitution of Fe^{2+} for Ca^{2+} creates a broad absorption centered at ~1.25–1.31 μm in feldspar [*Serventi et al.*, 2013] (Figure 2) that may be detectable where other mafic minerals are in abundances of <5% [*Ohtake et al.*, 2009; *Cheek et al.*, 2013]. These plagioclase-dominated materials have been found in the northern Hellas region, in the rims of large craters (including Holden), in a small valley in Xanthe Terra, and in the Nili Patera caldera of Syrtis Major; they are often associated with hydrated minerals, such as kaolinite, Fe/Mg-smectite, and hydrated silica [*Carter and Poulet*, 2013; *Wray et al.*, 2013].

3.2.4. Pyroxene

Besides plagioclase, pyroxene comprises the other dominant component of the igneous Martian crust [*Bandfield et al.*, 2000; *Bandfield*, 2002]. Pyroxene spectra display broad diagnostic absorptions near 1 μm and 2 μm that result from crystal field transitions of iron in octahedral coordination [*Burns*, 1993]. In low-calcium pyroxene (LCP), these bands are centered near 0.9 and 1.8 μm, while in high-calcium pyroxene (HCP), they are centered near 1.05 and 2.3 μm (Figure 2). LCP has been identified only in Noachian-aged terrains, suggesting the early Mars mantle was depleted in aluminum and calcium [*Mustard et al.*, 2005]. A systematic study of the composition of crater central peaks indicates that the ancient crust may have been largely composed of dunite and pyroxenite, formed through fractional crystallization, and was moderately iron rich and calcium poor [*Skok et al.*, 2012].

3.3. Sulfates

Secondary alteration of the crust through circulation of acidic groundwater, alteration of primary minerals through acidic rain and/or frost, or evaporation of standing bodies of water/brines may have lead to the precipitation of sulfate-bearing deposits [*Gendrin et al.*, 2005] and provide a record of past aqueous environments on Mars. Significant sulfate signatures occur in Valles Marineris in interior layered deposits on

the floor of the canyon system [*Gendrin et al.*, 2005; *Roach et al.*, 2009, 2010b; *Le Deit et al.*, 2010] and related chaos regions [*Lichtenberg et al.*, 2010], and in Meridiani Planum and surrounding regions of Arabia [*Arvidson et al.*, 2005; *Wray et al.*, 2009b; *Wiseman et al.*, 2010]. The dunes that surround the northern polar ice cap are dominated by the sulfate gypsum [*Langevin et al.*, 2005; *Massé et al.*, 2010, 2012].

Polyhydrated sulfate spectra display an absorption near 1.9 μm due to a combination of water molecule stretching and bending vibrations, whereas monohydrated sulfates have an absorption near 2.1 μm due to water vibrational combinations that shifts with cation (i.e., the absorption for Mg-kieserite occurs at a longer wavelength than Fe-szomolnokite) [*Cloutis et al.*, 2006]. Both polyhydrated and monohydrated sulfates exhibit a feature at 2.4 μm due to water combinations and/or overtones [*Cloutis et al.*, 2006] (Figure 3). Polyhydrated sulfates are challenging to identify unambiguously as the 1.4, 1.9, and 2.4 um absorptions can also be found in other families of hydrous minerals. Those species of sulfates with distinct spectral characteristics that have been detected include kieserite [*Gendrin et al.*, 2005], jarosite [*Farrand et al.*, 2009], bassanite [*Wray et al.*, 2010], gypsum [*Gendrin et al.*, 2005], alunite [*Swayze et al.*, 2008], and an unnamed iron-rich hydroxylated sulfate not known to occur naturally on Earth [*Lichtenberg et al.*, 2010]. Polyhydrated sulfates that may be stable on the surface of Mars and are likely candidates for the observed spectra include epsomite, hexahydrite, amorphous Mg-sulfate, and starkeyite [*Chipera and Vaniman*, 2007; *Wang et al.*, 2009].

3.4. Phyllosilicates

A variety of phyllosilicates including Al-micas, Al- and Fe/Mg-smectites, and kaolin-, serpentine-, chlorite-, and prehnite-group phyllosilicates have been identified on Mars in the most ancient Noachian crust. Phyllosilicate composition and geomorphic evidence can constrain the environmental formation of these phases. On Mars, these include low-grade metamorphic, hydrothermal, diagenetic, pedogenic, and detrital settings of formation and/or deposition [e.g., *Bishop et al.*, 2008; *Milliken and Bish*, 2010; *Ehlmann et al.*, 2011a; *Viviano et al.*, 2013a].

3.4.1. Al-Phyllosilicates

A variety of Al-rich phyllosilicates are observed, including Al smectites (e.g., montmorillonite and beidellite) with variable spectral characteristics, kaolinite-group phyllosilicates, and Al-micas, which may include illite, muscovite, and margarite. Kaolinite has a prominent 1.4 μm feature due to vibrations of hydroxyl groups and a doublet at 2.2 μm (centered at 2.16 and 2.21 μm) from a combination of vibrations of Al-OH [*Clark et al.*, 1990]. Both Al smectites and Al-micas exhibit a 2.2 μm band, but the micas can be discriminated through additional bands at 2.26 μm, 2.35 μm, and/or 2.44 μm from stretch and bend combination Al-OH bonds [*Clark et al.*, 1990] (Figure 4).

Al-phyllosilicates are particularly prevalent in Mawrth Vallis and the greater Arabia Terra region, where Al-smectite and kaolinite are present in the upper phyllosilicate-bearing unit of the light-toned rocks surrounding the outflow channel, and Fe-phyllosilicates are found in the lower units suggesting a pedogenic origin [*Bishop et al.*, 2008]. Similar stratigraphic sequences of Al-clays overlying Fe/Mg clays are found in the walls of Valles Marineris and in Thaumasia Planum [*Murchie et al.*, 2009; *Le Deit et al.*, 2012], Eridania Basin [*Noe Dobrea et al.*, 2008], Noctis Labyrinthus [*Weitz et al.*, 2011], Nili Fossae [*Ehlmann et al.*, 2009], and in Noachis Terra [*Wray et al.*, 2009a], suggesting formation via surface weathering. Al-micas are often associated with craters [*Ehlmann et al.*, 2009; *Carter et al.*, 2013b], which may imply the diagenetic transformation of Al smectites to illite [*Milliken and Bish*, 2010; *Bristow and Milliken*, 2011].

3.4.2. Fe/Mg-Phyllosilicates

Fe/Mg-bearing phyllosilicates are by far the most common hydrous mineral on Mars [*Carter et al.*, 2013b] and include Fe-smectite (e.g., nontronite), Mg-smectite (e.g., saponite), serpentine, talc-bearing material, chlorite, and prehnite. Fe/Mg-phyllosilicates are identified through structural H_2O and OH absorption features at 1.4 μm, a 1.9 μm feature due to structural H_2O, and a ~2.28–2.32 μm feature that will shift to longer wavelengths as Mg is exchanged for Fe [*Clark et al.*, 1990] (Figure 4). Although both exhibit 2.31 and 2.39 μm absorption bands, talc may be distinguished in the laboratory setting from Mg-smectite by its lack of interlayer H_2O (narrowing the 1.4 μm feature and eliminating the 1.9 μm feature), and in natural settings (where mixing with hydrated phases may occur) by a drop in the local continuum and the reflectance at 2.35 μm (between the 2.31 and 2.39 μm absorption bands) [*Viviano et al.*, 2013a]. The CRISM type spectrum for talc indeed displays mixing with other hydrated phases as indicated by a strong 1.9 μm feature. Chlorites display a strong 2.33–2.35 μm absorption resulting from the Mg-OH bond, where increasing iron to

magnesium will shift this band to longer wavelengths, plus weaker features at 2.25–2.26 μm due to Al, Fe-OH or Al,Mg-OH [*King and Clark*, 1989]. Similarly, the diagnostic feature for prehnite is between 2.35 and 2.36 μm; however, the presence of an absorption band at 1.48 μm distinguishes it from Fe-rich chlorite. Serpentine is identified through an absorption centered at 2.32 μm and 2.51 μm from Mg-OH or metal-OH combination tones, a diagnostic weaker band at ~2.1 μm, and OH overtones at 1.39 μm. Good signal-to-noise ratio must be present to detect the shallow, but diagnostic ~2.1 μm feature, which likely contributes to the scarcity of definitive observations of serpentine.

Chlorites are often associated with craters [*Ehlmann et al.*, 2009; *Carter et al.*, 2013b], which are consistent with the diagenetic transformation of Mg-smectite to chlorite [*Milliken and Bish*, 2010; *Viviano et al.*, 2013a]. The presence of prehnite is of particular interest on Mars, as it forms under specific hydrothermal or metamorphic conditions [*Ehlmann et al.*, 2009] at elevated temperatures (200–350°C) and constrained pressures (<3 kbar) [*Schiffman and Day*, 1999]. Fe/Mg-phyllosilicates are found in a variety of geologic settings, including stratified deposits (e.g., Mawrth Vallis), exposed through impact craters (e.g., throughout the Tyrrhena Terra region), in outcrops of exposed crust, and less often in alluvial fans or deltas [*Ehlmann et al.*, 2011b; *Carter et al.*, 2013b]. Thus, far serpentine has been observed to the west of Isidis Basin in Nili Fossae, in ancient terrain exposed to the south of Valles Marineris in Claritas Rise, and associated with several southern highland impact craters [*Ehlmann et al.*, 2010].

3.5. Carbonates

Carbonate deposits are an expected product from the interaction of water and basalt in a CO_2-rich atmosphere and would provide a sink for additional atmospheric CO_2 predicted for early Mars [*Pollack et al.*, 1987; *Catling*, 1999]. The identification of carbonates is also important for constraining fluid composition, as carbonates are formed and preserved only under neutral-to-alkaline conditions. Carbonates are identified through paired ~2.3 and ~2.5 μm features due to C-O bond vibration overtones, where Fe/Ca carbonates absorptions are centered at 2.33 and 2.53 μm, and Mg-rich carbonates are shifted to 2.30 and 2.51 μm [*Gaffey*, 1987] (Figure 5). As these absorption features may overlap with other phyllosilicates and zeolites, both absorption features must be present for definitive identification. Although CRISM data in the 3–4 μm range has a signal-to-noise ratio 4 times lower than at wavelengths <2.7 μm, significant second-order leaked light, and a probable detector artifact at 3.18 μm, diagnostic absorptions at 3.45 μm and 3.9 μm, while often weak, can also help confirm the presence of carbonates in CRISM data [*Murchie et al.*, 2007; *Ehlmann et al.*, 2008, 2009] (Figure 5). Carbonates have been identified through orbital observations in Nili Fossae [*Ehlmann et al.*, 2008, 2009], and throughout Tyrhenna Terra to the south of Isidis Basin and Syrtis Major [*Ehlmann et al.*, 2008; *Michalski and Niles*, 2010; *Wray et al.*, 2011a].

3.6. Halides and Other Hydrated Silicates
3.6.1. Hydrated Silica

Hydrated silica can form through several abiotic pathways: (1) precipitation from a solution: typically opal-A (noncrystalline) in chemical weathering systems, or chalcedony (micro/cryptocrystalline) in hydrothermal systems, (2) as a diagenetic alteration product: typically opal-CT (paracrystalline) through the diagenetic alteration of an opal-A precursor, or (3) as a replacement mineral: typically opal-A or opal-CT precipitating as nodules in limestones or dolostones [see *Smith et al.*, 2013, and references therein]. Hydrated silica exhibits absorption bands at 2.21–2.22 μm due to Si-OH combination tones, 2.26 μm due to H-bound Si-OH, 1.91 μm due to structural H_2O, and 1.4 μm due to structural H_2O and OH [*Stolper*, 1982] (Figure 6). Increasing crystallinity of hydrated silica will shift the ~1.4 μm band center to longer wavelengths (from 1.38 to 1.42 μm) and will increase the 1.91/1.96 μm band depth ratio [*Rice et al.*, 2013].

Hydrated silica deposits have been observed as layered deposits in the plains surrounding Valles Marineris [*Milliken et al.*, 2008], in aeolian dunes and ripples within and surrounding Antoniadi and Isidis basins [*Ehlmann et al.*, 2009; *Smith and Bandfield*, 2012], in Toro crater along the northern edge of the Syrtis Major volcanic plains [*Marzo et al.*, 2010], in the Nili Patera caldera of Syrtis Major [*Skok et al.*, 2010a], in the intercrater plains of Terra Sirenum [*Wray et al.*, 2011b], in the upper Al/Si-rich unit of the Mawrth Vallis stratigraphy [*Bishop et al.*, 2008], and in Noctis Labyrinthus [*Weitz et al.*, 2011]. These outcrops display a varying degree of silica crystallinity from noncrystalline (hydrated glass) to weakly crystalline (opal) to crystalline (quartz) [*Smith et al.*, 2013], suggesting the deposits experienced different styles or degrees of alteration.

3.6.2. Epidote

Prehnite-bearing assemblages suggest that only sub-greenschist metamorphic facies conditions were met on Mars [*Ehlmann et al.*, 2011a]. However, a spectral end-member extraction algorithm has been used to identify epidote on a crater floor in Hesperia Planum and near olivine and serpentine detections in Nili Fossae, indicating a higher grade metamorphism existed [*Carter et al.*, 2013a]. While the major 2.34 and 2.25 μm bands of epidote are spectrally similar to mixtures including calcite, chlorite, and illite and may be difficult to distinguish [*Dalton et al.*, 2004], the presence of a minor band at 1.55 μm in the extracted CRISM spectra is only consistent with laboratory spectra of epidote [*Carter et al.*, 2013a]. The 1.55 μm band is weak at best in CRISM ratioed I/F spectra, and thus, perhaps the confidence in the identification of this phase as epidote is lower than in other phases presented in this work. This is important to note, as the presence of epidote-bearing assemblages would suggest that rock types exist on Mars that are known to form in convergent plate margins on Earth [*Ehlmann et al.*, 2011a]. This would be inconsistent with the more readily accepted view that Mars is a single-plate planet, where a stagnant lid model [*Schubert et al.*, 2001] best explains volcanic production rates [e.g., *Breuer*, 2003], although other workers have suggested incipient or abortive plate tectonics on early Mars [e.g., *Yin*, 2012].

3.6.3. Zeolites

Zeolites originate in a variety of environments, including in alkaline waters, as alteration products of volcanic glasses, and in low-temperature hydrothermal environments [*Eugster*, 1980; *Sheppard and Hay*, 2001; *Weisenberger and Selbekk*, 2008]. Some zeolite spectra are spectrally very similar to polyhydrated sulfates, dominated by a large drop around 2.4 μm, 1.9 μm, and 1.4 μm due to bound water [*Cloutis*, 2002]. While most zeolites cannot easily be differentiated from polyhydrated sulfates, the zeolite analcime is quite distinct and displays an additional characteristic strong absorption at 2.5 μm and a weaker absorption at 1.79 μm apparent in CRISM data [*Ehlmann et al.*, 2009]. Other types of spectrally distinct zeolites such as natrolite, which has multiple H_2O-related sharp absorptions throughout the SWIR, have not yet been identified on Mars. TES spectra indicates that zeolite may be a significant component of Mars dust [*Ruff*, 2004], although the exact composition of the dust remains a subject of debate. Analcime has been unambiguously identified in several craters near Antoniadi basin in west and central Nili Fossae [*Ehlmann et al.*, 2009; *Viviano et al.*, 2013a] and in the southern highlands in a crater in southeast Cimmeria Terra [*Wray et al.*, 2009a].

3.6.4. Chlorides

Chlorides commonly precipitate from the evaporation of surface waters (saline lakewater) or from hydrothermal brines in the subsurface. They may also be formed during volcanic outgassing as fumarolic sublimates. Chloride deposits are identified in plains sediments in relatively flat areas of intercrater plains and crater floors and are often associated with phyllosilicate-bearing assemblages. Chlorides have unusually high apparent emissivity in the thermal infrared with a spectral downward slope toward lower wave number [*Osterloo et al.*, 2008] and lack diagnostic absorption features in the visible and near-infrared. Compared to other surface materials detected with CRISM, chlorides display a characteristic combination of a bluer slope in the VNIR, a redder slope in the IR (lacking the negative infrared slope characteristic of mixtures of dust and mafics), and a much weaker 3 μm H_2O feature apparently due to its anhydrous nature [*Murchie et al.*, 2009]. It is therefore possible to differentiate this material using CRISM spectra [e.g., *Glotch et al.*, 2010] based on these unique characteristics (Figure 6).

4. Revised CRISM Spectral Parameters

Parameterizing CRISM spectral data has proven to be a highly successful method of collapsing spectral variation within a scene into a limited number of dimensions. Initial versions of CRISM summary products [*Pelkey et al.*, 2007] have been incorporated into the CRISM Analysis Toolkit (CAT) and standard CRISM processing by the scientific community at large and have been established as an effective tool for rapid assessment and visualization of an information-rich data set. Revised parameters presented here will be integrated into a forthcoming version of the CAT. The following sections summarize the most commonly used functional forms and the mathematical rationales behind the majority of the parameters.

4.1. Band Depth Parameter

One of the most commonly used parameterizations of spectral data is a band (absorption) depth calculation [*Clark and Roush*, 1984], illustrated in Figure 7a. In this formulation, the reflectance at the center wavelength
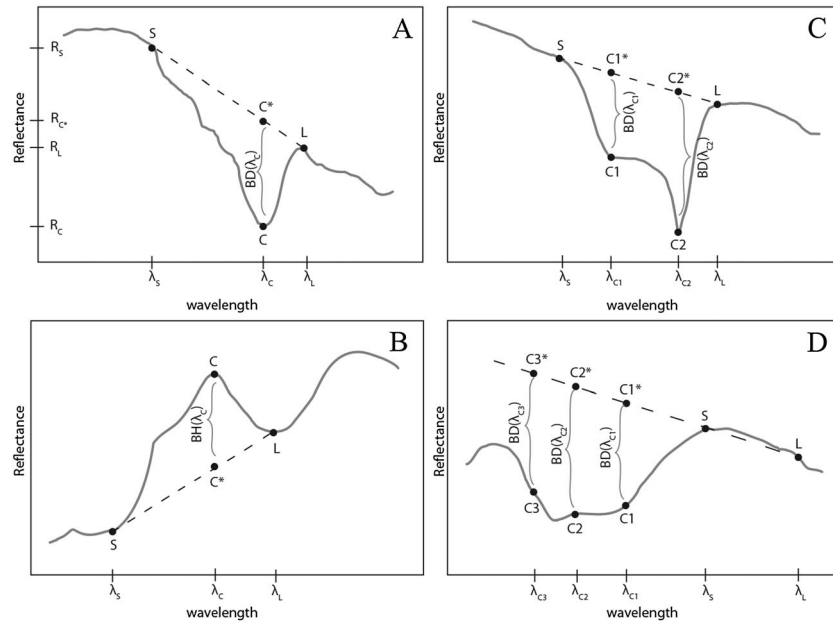
Figure 7. (a–d) A visual representation of several spectral parameter formulations using idealized spectra. The solid line is a hypothetical spectrum with the generalized spectral feature superimposed on the sloped continuum. The dashed line indicates a continuum fit across the absorption band by which a reflectance point along the continuum is calculated. See sections 4.1–4.4 for a description of each formulation.

(λ_C) is represented as R_C. The depth of the absorption, or band depth, is calculated by first deriving R_{C*}, or what the reflectance would be along an interpolated continuum at the same wavelength, from two longer and shorter wavelength points along the continuum (λ_S, R_S and λ_L, R_L). This can be expressed as the following:

$$R_{C*} = aR_S + bR_L, \text{ where} \tag{1}$$

$$a = 1 - b \text{ and } b = \frac{\lambda_C - \lambda_S}{\lambda_L - \lambda_S}. \tag{2}$$

The band depth, BD(λ_C), is calculated as 1 minus a ratio of the reflectance at R_C to R_{C*}, expressed as follows:

$$\text{BD}(\lambda_C) = 1 - \frac{R_C}{R_{C*}} = 1 - \frac{R_C}{aR_S + bR_L}. \tag{3}$$

The weighting parameters a and b (equations (1) and (2)) are particularly important for accurately representing the band depth of asymmetric absorption features in the cases where λ_C is not centered between λ_S and λ_L.

4.2. Inverse Band Depth Parameter

There are several situations where it is beneficial to characterize the "height" of an inflection in the spectrum, relative to an assumed underlying continuum. This calculation could be considered a "band height," BH(λ_C), where the inverse of the band depth is calculated as follows:

$$\text{BH}(\lambda_C) = 1 - \frac{R_{C*}}{R_C} = 1 - \frac{aR_S + bR_L}{R_C}. \tag{4}$$

This type of parameterization, represented in Figure 7b may be useful in instances where two defining absorption features overlap in the characteristic spectrum, with relatively minimal absorbing features occupying the wavelength space between. One example is at 0.6 μm, between stronger absorptions at 0.53 and 0.66 μm due to hematite.
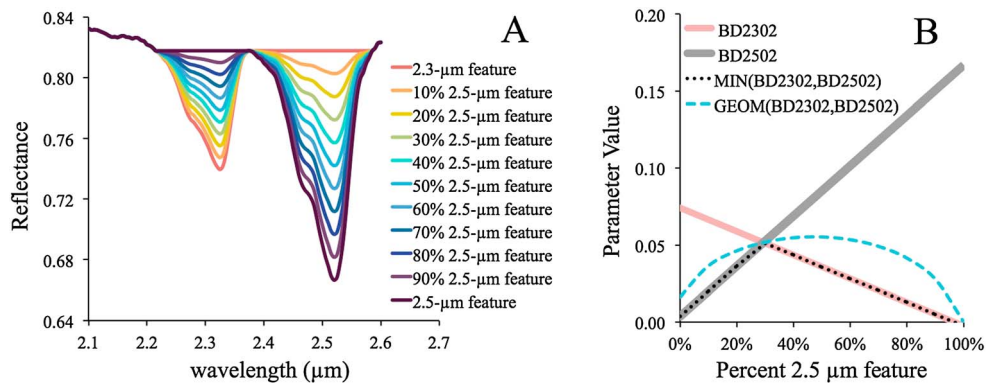
Figure 8. A model using magnesite (sample CACB03, RELAB) spectral absorption features at 2.3 and 2.5 μm and a flat continuum to test two-band spectral parameter formulations. (a) A linear mixing model inversely varying the depths of the 2.3 and 2.5 μm feature of the magnesite spectrum at 10% intervals. (b) The resulting spectral parameter values as a function of 2.3 and 2.5 μm band depth. See section 4.3 for a comparison between a minimum (MIN) formulation and a geometric mean (GEOM).

4.3. Doublet and Two-Band Parameters

There are some cases where a spectral feature of interest contains a doublet (two absorption features so close in wavelength that there is overlap in the "wings" of the features), or two (dual) absorption features that must be present for the identification of a particular spectral signature (Figure 7c). In these cases, the parameter must combine information from both of the band depths at λ_{C1} and λ_{C2} into a single value. Historically, this has been accomplished through a geometric mean (GEOM) (e.g., BDCARB in *Pelkey et al.* [2007]) and is calculated as follows:

$$
\begin{aligned}
\text{GEOM}(\text{BD}(\lambda_{C1}) \text{ and } \text{BD}(\lambda_{C2})) &= \sqrt{(\text{BD}(\lambda_{C1}))(\text{BD}(\lambda_{C2}))} \\
&= \sqrt{\left(1 - \frac{R_{C1}}{a_1 R_S + b_1 R_L}\right)\left(1 - \frac{R_{C2}}{a_2 R_S + b_2 R_L}\right)}.
\end{aligned}
\tag{5}
$$

However, the geometric mean formulation has a major limitation: if *both* band depths have negative values, i.e., the reflectance at the wavelength of interest is greater than the interpolated continuum, then the geometric mean value will be high, yielding a false positive. Instead of a geometric mean of the two band depths of interest, we employ a minimum (MIN) calculation, where the minimum (min) of the two band depths is reported:

$$
\text{MIN}(\text{BD}(\lambda_{C1}) \text{ and } \text{BD}(\lambda_{C2})) = \min[\text{BD}(\lambda_{C1}), \text{BD}(\lambda_{C2})].
\tag{6}
$$

In this more rigorous case, only those spectra with both absorption features present will result in a positive value. The geometric mean and the minimum calculation have different sensitivities as the relative difference in band depths varies (Figure 8). As the band depths of the two absorptions converge in value, $\text{BD}(\lambda_{C1}) \approx \text{BD}(\lambda_{C2})$, the geometric mean and minimum will also converge (intersection point, Figure 8b). If $\text{BD}(\lambda_{C1})$ is very shallow and $\text{BD}(\lambda_{C2})$ is much deeper (or vice versa), a geometric mean will produce a value much greater than the minimum calculation. In the case of carbonates, we expect both absorption bands at 2.3 and 2.5 μm to have relatively similar strengths. So, if a spectrum has a strong 2.3 feature and a very weak 2.5 feature, it will have a relatively larger value if the geometric mean is calculated. Therefore, we prefer the minimum calculation to a geometric mean, as it is robust against the case of negative band depth values and does not skew the resulting spectral parameter if only one of the two absorptions dominates the spectrum.

4.4. Broad Band Parameters

Lastly, there are several cases where the phase of interest has a broad absorption feature (Figure 7d) that spans multiple wavelengths sampled by CRISM (even at CRISM survey mode spectral sampling at 53.4 nm).

Combining multiple band depths as a weighted average can capture such broad features and is calculated as follows:

$$\text{BD}(\lambda_{C1-CN}) = D_1(\text{BD}(\lambda_{C1})) + D_2(\text{BD}(\lambda_{C2})) + \dots + D_N(\text{BD}(\lambda_{CN})) = \sum_{i=1}^{N} D_i(\text{BD}(\lambda_{Ci})), \quad (7)$$

where D_N represents a weighting coefficient that may vary for each band depth. The sum of all weighting coefficients is unity. In practice, coefficients are determined empirically through trial and error to best discriminate the spectral signature of interest from other spectrally similar phases. This type of parameterization is particularly useful for characterizing broad absorptions relating to Fe mineralogy (e.g., primary mafic minerals). Figure 7d also illustrates a case where the interpolated continuum and wavelength position of the band center fall outside the range of R_S and R_L (the points used to define the interpolated continuum). In these cases, the generic formulation for band depth (equations (1)–(3)) is still applicable.

4.5. Hyperspectral Versus Multispectral Parameterization

A hyperspectral derivation of a parameter utilizes the fact that most mineralogical absorptions are spectrally broad relative to the CRISM hyperspectral wavelength sampling. Because there are typically several channels in the CRISM hyperspectral mode that fall within a given spectral feature of interest, they can be combined in order to minimize the effects of residual noise in the spectrum. This type of noise is often stochastic, so a spectral median (rather than a mean) behaves more robustly in the presence of random spikes in the spectrum. In Table 2, we report the number of channels that are medianed in order to calculate the reflectance at a particular wavelength (R####), as the "5." For multispectral formulations, the kernel widths cannot be utilized since only one or two channels often sample an absorption feature.

5. Browse Products, Noise Filtering, and Parameter Threshold Values

5.1. Browse Products

The results of the revised spectral parameter calculations as applied to a hyperspectral CRISM image can be combined and stretched to produce interpretable browse product images. Browse products are 8-bit scaled RGB color composites that display three-band combinations of thematically related summary products and provide high-level visualizations of the information content of the calibrated image cube. A list of the browse product names, their three-band components, and guidance for each browse product's color interpretation is provided in Table 3. Though each browse product is useful in its own right (see "Significance and Interpretation" section of Table 3), we will highlight several of the new browse products here to emphasize their utility beyond the traditional set defined in *Pelkey et al.* [2007]. As an example, two new browse products, PFM and PAL, are more sensitive to subtle variability in phyllosilicate species as compared to phyllosilicates detected with the original PHY product. The PFM product (RGB = BD2355, D2300, and BD2290) shows information related to Fe/Mg-phyllosilicates, where red/yellow colors may indicate the presence of prehnite or chlorite, and cyan colors commonly indicate Fe/Mg smectites. In the PHY product (RGB = D2300, D2200, and BD1900r2), all Fe/Mg-phyllosilicates are an indistinguishable red/magenta if they have hydration bands of comparable strength. The PAL product (RGB = BD2210_2, BD2190, and BD2165) shows information related to Al-OH materials, where Al smectites appear cyan and kaolin-group minerals are light/white in color. In the PHY product, all Al-OH phases are an indistinguishable green/cyan if they have hydration bands of comparable strength. The HYS product (RGB = MIN2250, BD2250, and BD1900r2) further differentiates between Si/Al-hydroxylated minerals, where hydrated silica appears a light red/yellow and Al-OH minerals appear cyan. Because of the interscene variability of the distribution of values in the summary products, each summary product is stretched individually, as described in section 5.3, before being converted to an 8-bit RGB channel component of the browse product.

5.2. Noise Filtering

A noise-reduction procedure has been implemented for the majority of the CRISM summary products. Most spectral parameters are continuum normalized, having the desirous effect of accentuating small spectral variations, but also the side effect of accentuating noise residuals that can compromise the resulting visualization products. To maximize the scientific utility of the summary products and derivative browse products, a custom noise remediation procedure is applied to the summary products. This procedure has

Table 2. Updated Summary Products[a]

#	Name	Status[b]	Parameter	Formulation	Kernel Width[c]	Rationale	Caveats
1	R770	✓	0.77 μm reflectance	$R770$	R770: 5	Higher value more dusty or icy	Sensitive to slope effects, clouds
2	RBR	✓	Red/blue ratio	$R770/R440$	R440: 5 R770: 5	Higher value indicates more npFeOx	Sensitive to dust in atmosphere
3	BD530	✗	0.53 μm band depth	$1 - \left(\dfrac{R530}{a*R716 + b*R440}\right)$	–	–	–
	BD530_2	✓	0.53 μm band depth	$1 - \left(\dfrac{R530}{a*R614 + b*R440}\right)$	R440: 5 R530: 5 R614: 5	Higher value has more fine-grained crystalline hematite	–
4	SH600	✗	0.6 μm shoulder height	$1 - \left(\dfrac{a*R530 + b*R709}{R600}\right)$	–	–	–
	SH600_2	✓	0.6 μm shoulder height	$1 - \left(\dfrac{a*R533 + b*R716}{R600}\right)$	R533: 5 R600: 5 R716: 3	Select ferric minerals (especially hematite and goethite) or compacted texture[d]	Sensitive to high opacity in atmosphere
5	SH770	✓	0.77 μm shoulder height	$1 - \left(\dfrac{a*R716 + b*R860}{R775}\right)$	R716: 3 R775: 5 R860: 5	Select ferric minerals, less sensitive to LCP than SH600_2	Sensitive to high opacity in atmosphere
6	BD640	✗	0.64 μm band depth	$1 - \left(\dfrac{R648}{a*R600 + b*R709}\right)$	–	Select ferric minerals (especially maghemite)	Obscured by VNIR detector artifact
	BD640_2	✓	0.64 μm band depth	$1 - \left(\dfrac{R624}{a*R600 + b*R760}\right)$	R600: 5 R624: 3 R760: 5	Select ferric minerals (especially maghemite)	Obscured by VNIR detector artifact
7	BD860	✗	0.86 μm band depth	$1 - \left(\dfrac{R860}{a*R800 + b*R984}\right)$	–	–	–
	BD860_2	✓	0.86 μm band depth	$1 - \left(\dfrac{R860}{a*R755 + b*R977}\right)$	R755: 5 R860: 5 R977: 5	Select crystalline ferric minerals (especially hematite)	–
8	BD920	✗	0.92 μm band depth	$1 - \left(\dfrac{R920}{a*R800 + b*R984}\right)$	–	–	–
	BD920_2	✓	0.92 μm band depth	$1 - \left(\dfrac{R920}{a*R807 + b*R984}\right)$	R807: 5 R920: 5 R984: 5	Crystalline ferric minerals and LCP	–
9	RPEAK1 *	✓	Reflectance peak 1	Wavelength where first derivative = 0 of fifth-order polynomial fit to reflectances at all valid VNIR wavelengths	–	Fe mineralogy (<0.75 suggests olivine, ~0.75 pyroxene, and >0.8 dust)	–
10	BDI1000VIS	✓	1 μm integrated band depth; VNIR wavelengths	Divide reflectances from R833 to R1023 by the modeled reflectance at RPEAK1, then integrate over (1 − normalized radiances) to get integrated band depth	–	Olivine, pyroxene, or Fe-bearing glass	–

Table 2. (continued)

#	Name	Status[b]	Parameter	Formulation	Kernel Width[c]	Rationale	Caveats
11	BDI1000IR	√	1 μm integrated band depth; IR wavelengths	Divide reflectances from R1045 to R1255 by linear fit from median R (of the 15) between 1.3 and 1.87 μm to median R between 2.43 and 2.6 μm extrapolated backward, then integrate over (1 − normalized radiances) to get integrated band depth	–	Crystalline Fe^{2+} silicates	–
12	R1330	√	IR albedo	$R1330$	R1330:11	IR albedo (ices > dust > unaltered mafics)	–
13	BD1300	√+	1.3 μm absorption associated with Fe^{2+} substitution in plagioclase	$1 - \left(\dfrac{R1320}{a*R1080 + b*R1750} \right)$	R1370: 5 R1432:15 R1470: 5	Plagioclase with Fe^{2+} substitution	Fe-Olivine can be > 0
	OLINDEX2	×	Detect broad absorption centered at 1 μm	$(RB1080*0.1) + (RB1210*0.1) + (RB1330*0.4) + (RB1470*0.4)$. Where $RB#### = (RC#### − R####)/RC ####$. RC denotes the value of a point at a wavelength of #### nm along a modeled line that follows the average slope of the spectrum. Slope for RC#### anchored at R1750 and R2400.	–	Olivines will be strongly > 0	HCP, Fe-phyllosilicates
14	OLINDEX3	√	Detect broad absorption centered at 1 μm	$RB1210*0.1 + RB1250*0.1 + RB1263*0.2 + RB1276*0.2 + RB1330*0.4$ Slope for RC#### anchored at R1750 and R1862.	R1210: 7 R1250: 7 R1263: 7 R1276: 7 R1330: 7 R1750: 7 R1862: 7	Olivines will be strongly > 0	HCP, Fe-phyllosilicates
	LCPINDEX	×	LCP index	$\left(\dfrac{R1330 − R1050}{R1330 + R1050} \right) * \left(\dfrac{R1330 − R1815}{R1330 + R1815} \right)$	–	Pyroxene is strongly +; favors LCP	–
15	LCPINDEX2	√+	Detect broad absorption centered at 1.81 μm	$RB1690*0.20 + RB1750*0.20 + RB1810*0.30 + RB1870*0.30$ Slope for RC#### anchored at R1560 and R2450.	R1560: 7 R1690: 7 R1750: 7 R1810: 7 R1870: 7 R2450: 7	Pyroxene is strongly +; favors LCP	–
	HCPINDEX	×	HCP index	$\left(\dfrac{R1470 − R1050}{R1470 + R1050} \right) * \left(\dfrac{R1470 − R2067}{R1470 + R2067} \right)$	–	Pyroxene is strongly +; favors HCP	LCP
16	HCPINDEX2	√+	Detect broad absorption centered at 2.12 μm	$RB2120*0.10 + RB2140*0.10 + RB2230*0.15 + RB2250*0.30 + RB2430*0.20 + RB2460*0.15$ Slope for RC#### anchored at R1690 and R2530.	R1810: 7 R2120: 5 R2140: 7 R2230: 7 R2250: 7 R2430: 7 R2460: 7 R2530: 7	Pyroxene is strongly +; favors HCP	LCP

Table 2. (continued)

#	Name	Status[b]	Parameter	Formulation	Kernel Width[c]	Rationale	Caveats
17	VAR	√	1.0–2.3 μm spectral variance	Fit a line from 1 to 2.3 μm and find variance of observed values from fit values by summing in quadrature over the intervening wavelengths	–	Ol and Px will have high values; (to be used with mafic indices)	Ices
18	ISLOPE1	√	Spectral slope 1	$\dfrac{R1815 - R2530}{W2530 - W1815}$	R1815: 5 R2530: 5	Ferric coating on dark rock	Shaded slopes illuminated by atmospheric scatter
19	BD1400	√	1.4 μm H_2O and –OH band depth	$1 - \left(\dfrac{R1395}{a*R1330 + b*R1467}\right)$	R1370: 5 R1432: 3 R1470: 5	Hydrated or hydroxylated minerals	–
20	BD1435	√	1.435 μm CO_2 ice band depth	$1 - \left(\dfrac{R1435}{a*R1370 + b*R1470}\right)$	R1370: 3 R1432: 1 R1470: 3	CO_2 ice, some hydrated minerals	–
	BD1500	x	1.5 μm H_2O ice band depth	$1 - \left(\dfrac{R1505 + R1558}{R1808 + R1367}\right)$	–	H_2O ice on surface or in atmosphere	–
21	BD1500_2	√	1.5 μm H_2O ice band depth	$1 - \left(\dfrac{R1525}{a*R1367 + b*R1808}\right)$	R1367: 5 R1525:11 R1808: 5	H_2O ice on surface or in atmosphere	–
	ICER1	x	CO_2 and H_2O ice band depth ratio	$R1510/R1430$	R1510: 5 R1430: 5	CO_2 H_2O ice mixtures; > 1 for more CO_2, < 1 for more water	–
22	ICER1_2	√	CO_2 and H_2O ice band depth ratio	$1 - \left(\dfrac{1 - BD1435}{1 - BD1500_2}\right)$	–	CO_2 H_2O ice mixtures; > 1 for more CO_2, < 1 for more water	–
	BD1750	x	1.7 μm H_2O band depth	$1 - \left(\dfrac{R1750}{a*R1550 + b*R1815}\right)$	–	Gypsum Alunite	–
23	BD1750_2	√	1.7 μm H_2O band depth	$1 - \left(\dfrac{R1750}{a*R1690 + b*R1815}\right)$	R1690: 5 R1750: 3 R1815: 5	Gypsum Alunite	–
	BD1900	x	1.9 μm H_2O band depth	$1 - \left(\dfrac{\frac{R1930 + R1985}{2}}{a*1875 + b*2067}\right)$	–	Bound molecular H_2O except monohydrated sulfates	–
24	BD1900_2	√+	1.9 μm H_2O band depth	$0.5*\left(1 - \left(\dfrac{R1930}{a*R1850 + b*R2067}\right)\right) + 0.5*\left(1 - \left(\dfrac{R1985}{a*R1850 + b*R2067}\right)\right)$	R1850: 5 R1930: 5 R1985: 5 R2046: 5	Bound molecular H_2O except monohydrated sulfates	–
	BD1900r	x	1.9 μm H_2O band depth	$1 - \left(\dfrac{R1908 + R1914 + R1921 + R1928 + R1934 + R1941}{R1862 + R1869 + R1875 + R2112 + R2120 + R2126}\right)$	–	H_2O	–

Table 2. (continued)

#	Name	Status[b]	Parameter	Formulation	Kernel Width[c]	Rationale	Caveats
25	BD1900r2	√+	1.9 μm H$_2$O band depth	$1 - \left(\dfrac{\frac{R1908}{RC1908} + \frac{R1914}{RC1914} + \frac{R1921}{RC1921} + \frac{R1928}{RC1928} + \frac{R1934}{RC1934} + \frac{R1941}{RC1941}}{\frac{R1862}{RC1862} + \frac{R1869}{RC1869} + \frac{R1875}{RC1875} + \frac{R2112}{RC2112} + \frac{R2120}{RC2120} + \frac{R2126}{RC2126}} \right)$ Slope for RC### anchored at R1850 and R2060.	–	H$_2$O	–
26	BDI2000	√	2 μm integrated band depth	Divide reflectances from R1660 to R2390 by linear fit from peak R (of 15) between 1.3 and 1.87 μm to R2530, then integrate over (1 − normalized radiances) to get integrated band depth	–	Pyroxene	Ices
	BD2100	×	2.1 μm shifted H$_2$O band depth	$1 - \left(\dfrac{\frac{R2120+R2130}{2}}{a*R1930+b*R2250} \right)$	–	H$_2$O in monohydrated sulfates	Alunite, Serpentine
27	BD2100_2	√+	2.1 μm shifted H$_2$O band depth	$1 - \left(\dfrac{R2132}{a*R1930+b*R2250} \right)$	R1930: 3 R2132: 5 R2250: 3	H$_2$O in monohydrated sulfates	Alunite, Serpentine
28	BD2165	√+	2.165 μm Al-OH band depth	$1 - \left(\dfrac{R2165}{a*R2120+b*R2230} \right)$	R2120: 5 R2165: 3 R2230: 3	Pyrophyllite Kaolinite group	Beidellite Allophane Imogolite
29	BD2190	√+	2.190 μm Al-OH band depth	$1 - \left(\dfrac{R2185}{a*R2120+b*R2250} \right)$	R2120: 5 R2185: 3 R2250: 3	Beidellite Allophane Imogolite	Kaolinite group
	DOUB2200H	×	2.16 μm Si-OH band depth and 2.21 μm H-bound Si-OH band depth (doublet)	$1 - \left(\dfrac{R2205+R2258}{R2172+R2311} \right)$	R2172: 5 R2205: 3 R2258: 3 R2311: 5	Opal and other Al-OH minerals	–
30	MIN2200	√+	2.16 μm Si-OH band depth and 2.21 μm H-bound Si-OH band depth (doublet)	$\text{minimum}\left[\left(1 - \left(\dfrac{R2165}{a*R2120+b*R2350}\right)\right), \left(1 - \left(\dfrac{R2210}{a*R2120+b*R2350}\right)\right) \right]$	R2120: 5 R2165: 3 R2120: 3 R2350: 5	Kaolinite group	–
	BD2210	×	2.21 μm Al-OH band depth	$1 - \left(\dfrac{R2210}{a*R2120+b*R2250} \right)$	–	Al-OH minerals	Gypsum, Alunite
31	BD2210_2	√	2.21 μm Al-OH band depth	$1 - \left(\dfrac{R2210}{a*R2165+b*R2250} \right)$	R2165: 5 R2210: 5 R2250: 5	Al-OH minerals	Gypsum, Alunite
32	D2200	√+	2.2 μm dropoff	$1 - \left(\dfrac{\frac{R2210}{RC2210} + \frac{R2230}{RC2230}}{2*\frac{R2165}{RC2165}} \right)$ Slope for RC### anchored at R1815 and R2430.	R1815: 7 R2165: 5 R2210: 7 R2230: 7 R2430: 7	Al-OH minerals	Chlorite, Prehnite

Table 2. (continued)

#	Name	Status[b]	Parameter	Formulation	Kernel Width[c]	Rationale	Caveats
33	BD2230	√+	2.23 μm band depth	$1 - \left(\dfrac{R2235}{a*R2210 + b*R2252}\right)$	R2210: 3 R2235: 3 R2252: 3	Hydroxylated ferric sulfate	Other Al-OH minerals
34	BD2250	√+	2.25 μm broad Al-OH and Si-OH band depth	$1 - \left(\dfrac{R2245}{a*R2120 + b*R2340}\right)$	R2120: 5 R2245: 7 R2340: 3	Opal and other Al-OH minerals	–
35	MIN2250	√+	2.21 μm Si-OH band depth and 2.26 μm H-bound Si-OH band depth	$\text{minimum}\left[\left(1 - \left(\dfrac{R2210}{a*R2165 + b*R2350}\right)\right),\ \left(1 - \left(\dfrac{R2265}{a*R2165 + b*R2350}\right)\right)\right]$	R2165: 5 R2210: 3 R2265: 3 R2350: 5	Opal	–
36	BD2265	√+	2.265 μm band depth	$1 - \left(\dfrac{R2265}{a*R2210 + b*R2340}\right)$	R2210: 5 R2265: 3 R2340: 5	Jarosite Gibbsite Acid-leached nontronite	–
37	BD2290	√	2.3 μm Mg,Fe-OH band depth/ 2.292 μm CO₂ ice band depth	$1 - \left(\dfrac{R2290}{a*R2250 + b*R2350}\right)$	R2250: 5 R2290: 5 R2350: 5	Mg,Fe-OH minerals; Also CO₂ ice	Mg-Carbonate
38	D2300	√	2.3 μm dropoff	$1 - \left(\dfrac{\frac{R2290}{RC2290} + \frac{R2320}{RC2320} + \frac{R2330}{RC2330}}{\frac{R2120}{RC2120} + \frac{R2170}{RC2170} + \frac{R2210}{RC2210}}\right)$ Slope for RC### anchored at R1815 and R2530.	R1815: 5 R2120: 5 R2170: 5 R2210: 5 R2290: 3 R2320: 3 R2330: 3 R2530: 5	Hydroxylated Fe,Mg silicates strongly > 0	Mg-Carbonate
39	BD2355	√	2.35 μm band depth	$1 - \left(\dfrac{R2355}{a*R2300 + b*R2450}\right)$	R2300: 5 R2355: 5 R2450: 5	Chlorite Prehnite Pumpellyite	Carbonate Serpentine
	SINDEX	×	Detects convexity at 2.29 μm due to 2.1 μm and 2.4 μm absorptions	$1 - \left(\dfrac{R2100 + R2400}{2*R2290}\right)$	–	Hydrated sulfates (mono and polyhydrated sulfates) will be > 1	Ices
40	SINDEX2	√+	Inverse lever rule to detect convexity at 2.29 μm due to 2.1 μm and 2.4 μm absorptions	$1 - \left(\dfrac{a*R2120 + b*R2400}{R2290}\right)$	R2120: 5 R2290: 7 R2400: 3	Hydrated sulfates (mono and polyhydrated sulfates) will be strongly > 0	Ices
	ICER2	×	2.7 μm CO₂ ice band	$R2530/R2600$	–	CO₂ versus water ice/soil; CO₂ will be > >1, water ice and soil will be ~1	–

Table 2. (continued)

#	Name	Status[b]	Parameter	Formulation	Kernel Width[c]	Rationale	Caveats
41	ICER2_2	√	2.7 μm CO2 ice band	$RB2600$ Slope for RC### anchored at R2456 and R2530.	R2456: 5 R2530: 5 R2600: 5	CO_2 versus water ice/soil; CO_2 will be strongly >0, water ice will be <0	–
	BDCARB	x	Carbonate overtone band depth, or metal-OH band	$1-\sqrt{\left(\dfrac{R2330}{a*R2230+b*R2390}\right)*\left(\dfrac{R2530}{c*R2390+d*R2600}\right)}$	–	Carbonates	Many hydroxylated silicate phases
42	MIN2295_2480	√+	Mg Carbonate overtone band depth and metal-OH band	$\mathrm{minimum}\left[\left(1-\left(\dfrac{R2295}{a*R2165+b*R2364}\right)\right),\ \left(1-\left(\dfrac{R2480}{a*R2364+b*R2570}\right)\right)\right]$	R2165: 5 R2295: 5 R2364: 5 R2480: 5 R2570: 5	Mg carbonates; both overtones must be present	Hydroxylated silicate + zeolite mixtures
43	MIN2345_2537	√+	Ca/Fe Carbonate overtone band depth and metal-OH band	$\mathrm{minimum}\left[\left(1-\left(\dfrac{R2345}{a*R2250+b*R2430}\right)\right),\ \left(1-\left(\dfrac{R2537}{a*R2430+b*R2602}\right)\right)\right]$	R2250: 5 R2345: 5 R2430: 5 R2537: 5 R2602: 5	Ca/Fe carbonates; both overtones must be present	Prehnite, Serpentine, Hydroxylated silicate + zeolite mixtures
	BD2500H	x	Mg Carbonate overtone band depth	$1-\left(\dfrac{R2500+R2510}{R2540+R2380}\right)$	–	Mg carbonates	Some zeolites
44	BD2500_2	√	Mg Carbonate overtone band depth	$1-\left(\dfrac{R2480}{a*R2364+b*R2570}\right)$	R2364: 5 R2480: 5 R2570: 5	Mg carbonates	Some zeolites
45	BD3000	√	3 μm H2O band depth	$1-\left(\dfrac{R3000}{R2530*\left(\frac{R2530}{R2210}\right)}\right)$	R2210: 5 R2530: 5 R3000: 5	Bound H_2O (accounts for spectral slope)	–
46	BD3100	√	3.1 μm H2O ice band depth	$1-\left(\dfrac{R3120}{a*R3000+b*R3250}\right)$	R3000: 5 R3120: 5 R3250: 5	H_2O ice	–
47	BD3200	√	3.2 μm CO2 ice band depth	$1-\left(\dfrac{R3320}{a*R3250+b*R3390}\right)$	R3250: 5 R3320: 5 R3390: 5	CO_2 ice	–
	BD3400	x	3.4 μm carbonate band depth	$1-\left(\dfrac{a*R3390+b*R3500}{c*R3250+d*R3630}\right)$	–	Ca/Fe carbonates	–
48	BD3400_2	√	3.4 μm carbonate band depth	$1-\left(\dfrac{R3420}{a*R3250+b*R3630}\right)$	R3250:10 R3420:15 R3630:10	Carbonates	–
	CINDEX	x	3.9 μm carbonate index	$\left(\dfrac{R3750+\frac{(R3750-R3630)}{(3750-3630)}*(3950-3750)}{R3950}\right)-1$	–	Carbonates will be > 'background' values >0	–

Table 2. (continued)

#	Name	Status[b]	Parameter	Formulation	Kernel Width[c]	Rationale	Caveats
49	CINDEX2	√+	Inverse lever rule to detect convexity at 3.6 μm due to 3.4 μm and 3.9 μm absorptions	$1 - \left(\dfrac{a*R3450 + b*R3875}{R3610} \right)$	R3450: 9 R3610:11 R3875: 7	Carbonates will be > 'background' values > 0	–
				Atmospheric Parameters and Browse Product Components			
50	R440	√	0.44 μm reflectance	R440	R440: 5	Clouds/Hazes	–
51	R530	√	0.53 μm reflectance	R530	R530: 5	TRU browse product component	–
52	R600	√	0.60 μm reflectance	R600	R600: 5	TRU browse product component	–
53	IRR1	√	IR ratio 1	R800/R997	R800: 5 R997: 5	Aphelion ice clouds (>1) versus seasonal or dust (<1)	–
54	R1080	√	1.08 μm reflectance	R1080	R1080: 5	FAL browse product component	–
55	R1506	√	1.51 μm reflectance	R1506	R1506: 5	FAL browse product component	–
56	R2529	√	2.53 μm reflectance	R2529	R2529: 5	TAN browse product component	–
57	BD2600	√	2.6 μm H$_2$O band depth	$1 - \left(\dfrac{R2600}{a*R2530 + b*R2630} \right)$	R2530: 5 R2600: 5 R2630: 5	H$_2$O vapor (accounts for spectral slope)	–
58	IRR2	√	IR ratio 2	R2530/R2210	R2210: 5 R2350: 5	Aphelion ice clouds versus seasonal or dust	–
59	IRR3	√	IR ratio 3	R3500/R3390	R3390: 7 R3500: 7	Aphelion ice clouds (higher values) versus seasonal or dust	–
60	R3920	√	3.92 μm reflectance	R3920	R3920: 5	IC2 browse product component	–

[a]R#### indicates reflectance at a particular wavelength W#### (nm). Formulations often take the form of equations (3)–(6), where a and b may be solved for using equation (2). Those with a status of "x" indicate retired parameters.
[b]Status definitions: x = retired parameter, √ = retained slightly modified parameter, √+ = significantly modified or new parameter.
[c]See section 4.5 for a description of "kernel width."
[d]See *Fischer and Pieters* [1993].

Table 3. Updated Browse Product Definitions and Descriptions

Abbreviation	RGB Components	Significance and Interpretation
	VNIR Browse Products	
TRU	R600 R530 R440	From "true color." An enhanced true color representation of the scene, derived from I/F after correction for atmospheric and photometric effects.
VNA	R770 R770 R770	From "VNIR albedo." Shows photometrically corrected I/F at 770 nm and may be used to correlate spectral variations with morphology.
FEM	BD530_2 SH600_2 BDI1000VIS	From "Fe minerals." Shows information related to Fe minerals and represents the curvature in the visible and near-infrared wavelengths related to iron. FEM is particularly sensitive to ferric and ferrous mineral absorptions, as well as negative slopes due to dust coatings or compacted dust texture. Red colors indicate nanophase or crystalline ferric oxides, green colors are usually a result of textural effects, and blue colors are usually dust-free or more mafic surfaces.
FM2	BD530_2 BD920_2 BDI1000VIS	From "Fe minerals, second version." Shows complementary information related to Fe minerals. The FM2 browse product is particularly sensitive to olivine and pyroxene, as well as nanophase ferric oxide and crystalline ferric or ferrous minerals. Red colors indicate the presence of nanophase ferric oxides, green colors suggest coarser-grained Fe minerals (particularly low-Ca pyroxene), and blue colors are often dust-free or more mafic surfaces.
	Joined Browse Product	
TAN	R2529 IRA R770	From "tandem." An enhanced visible to infrared false color representation of the scene.
	IR Browse Products	
IRA	R1300 R1300 R1300	From "IR albedo." Shows photometrically corrected I/F at 1330 nm and may be used to correlate spectral variations with morphology.
FAL	R2529 R1506 R1080	From "false color." An enhanced infrared false color representation of the scene. The wavelengths chosen highlight differences between key mineral groups. Red/orange colors are usually characteristic of olivine-rich material, blue/green colors often indicate clay, green colors may indicate carbonate, and gray/brown colors often indicate basaltic material.
MAF	OLINDEX3 LCPINDEX2 HCPINDEX2	From "mafic mineralogy." Shows information related to mafic mineralogy. Olivine and Fe-phyllosilicate share a 1.0–1.7 μm bowl-shaped absorption and will appear red in the MAF browse product. Low- and high-Ca pyroxene display additional ~2.0 μm absorptions and appear green/cyan and blue/magenta, respectively.
HYD	SINDEX2 BD2100_2 BD1900_2	From "hydrated mineralogy." Shows information related to bound water in minerals. Polyhydrated sulfates have strong 1.9 μm and 2.4 μm absorption bands, and thus appear magenta in the HYD browse product. Monohydrated sulfates have a strong 2.1 μm absorption and a weak 2.4 μm absorption band, and thus appear yellow/green in the HYD browse product. Blue colors are indicative of other hydrated minerals (such as clays, hydrated silica, carbonate, or zeolite).
PHY	D2300 D2200 BD1900r2	From "phyllosilicates." Shows information related to hydroxylated minerals including phyllosilicates. Fe/Mg-OH bearing minerals (e.g., Fe/Mg-phyllosilicates) will appear red, or magenta when hydrated. Al/Si-OH bearing minerals (e.g., Al-phyllosilicates or hydrated silica) will appear green, or cyan when hydrated. Blue colors are indicative of other hydrated minerals (such as sulfates, hydrated silica, carbonate, or water ice).
PFM	BD2355 D2300 BD2290	From "phyllosilicates with Fe and Mg." Shows information related to cation composition of hydroxylated minerals including Fe/Mg-phyllosilicate. Red/yellow colors indicate the presence of prehnite, chlorite, epidote, or Ca/Fe carbonate, while cyan colors indicate the presence of Fe/Mg smectites or Mg carbonate.
PAL	BD2210_2 BD2190 BD2165	From "phyllosilicates with Al." Shows information related to cation composition of hydroxylated minerals including Al-phyllosilicate and hydrated silica. Red/yellow colors indicate the presence of Al smectites or hydrated silica, cyan colors may indicate the alunite, and light/white colors indicate the presence of kaolinite group minerals.
HYS	MIN2250 BD2250 BD1900r2	From "hydrated silica." Shows information related to Si/Al-hydroxylated minerals that can be used to differentiate between hydrated silica and Al-phyllosilicates. Light red/yellow colors indicate the presence of hydrated silica, whereas cyan colors indicate Al-OH minerals. Additionally, jarosite will appear yellow. Blue colors are indicative of other hydrated minerals (such as sulfates, clays, hydrated silica, carbonate, or water ice).
ICE	BD1900_2 BD1500_2 BD1435	From "ices." Shows information related to water or carbon dioxide frost or ice. CO_2 frost or ice displays a sharp 1.435 μm absorption and thus appears blue in the ICE browse product. Water ice or frost has a strong 1.5 μm absorption and thus appears green in the ICE browse product. Red colors are indicative of hydrated minerals (such as sulfates, clays, hydrated silica, carbonate, or water ice).

Table 3. (continued)

Abbreviation	RGB Components	Significance and Interpretation
IC2	R3920 BD1500_2 BD1435	From "ices, version 2." Shows complementary information related to water or carbon dioxide frost or ice. CO_2 frost or ice displays a sharp 1.435 μm absorption and thus appears blue in the IC2 browse product. Water ice or frost has a strong 1.5 μm absorption and thus appears green in the IC2 browse product. The reflectance at 3920 nm is a proxy for silicates, which are more reflectance than ices at 3.9 μm, so red colors represent ice-free surfaces.
CHL	ISLOPE BD3000 IRR2	From "chloride." Shows information related to inferred chloride deposits detected from Thermal Emission Imaging System (THEMIS) data and spatially associated hydrated mineral deposits. Of the THEMIS-based chloride detections studied to date, these surfaces have a relatively positive near-infrared spectral slope and are comparatively desiccated, so chlorides appear blue in the CHL browse product. Yellow/green colors are indicative of hydrated minerals, especially phyllosilicates.
CAR	D2300 BD2500H2 BD1900_2	From "carbonates." Shows information related to Mg carbonate minerals. Blueish- or yellowish-white colors indicate Mg carbonates, while red/magenta colors indicate Fe/Mg-phyllosilicates. Blue colors are indicative of other hydrated minerals (such as sulfates, clays, hydrated silica, or carbonate).
CR2	MIN2295_2480 MIN2345_2537 CINDEX2	From "carbonates, version 2." Shows information distinguishing carbonate minerals. Red/magenta colors indicate Mg carbonates, while green/cyan colors indicate Fe/Ca carbonates.

some heritage in the CRISM hyperspectral data filtering procedure [*Seelos et al.*, 2009] implemented in version 3 of the CRISM calibration pipeline. It has been modified to operate on individual parameter bands, rather than hyperspectral I/F data. The filtering procedure identifies spurious pixels using a statistical outlier test applied to an iterative sampling kernel. Pixels that are flagged as outliers are subsequently interpolated from neighboring nonspurious data elements.

5.3. Parameter Threshold Values and Stretching

The distribution of values in each summary product image varies based on the mathematical characteristics of the parameter formulation, the spectral variability and areal distribution of target material captured in the
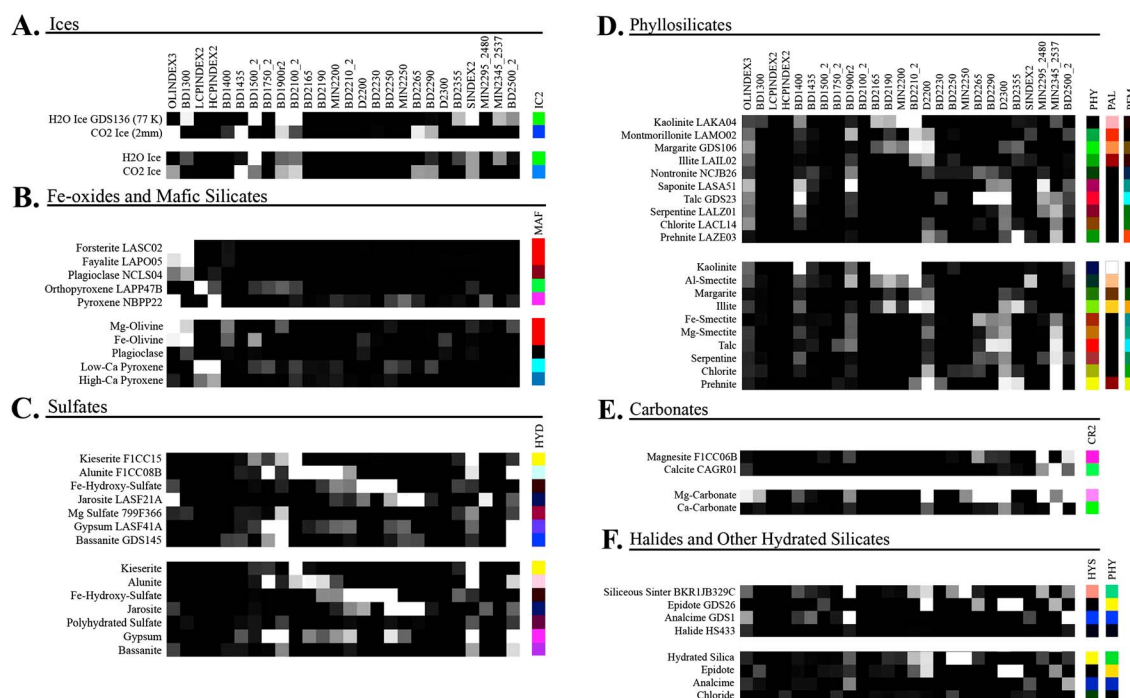

Figure 9. Summary product sensitivity matrices for each type spectra class (A–F). The top set of rows of each class show the response of analog laboratory material and the bottom set of rows show the corresponding response of CRISM MICA type spectra for each spectral parameter (columns). Each parameter is linearly scaled and has a fixed lower stretch limit of zero (black indicates a band depth at or below zero) and an upper limit of the highest response of the distribution (white). To the right of each matrix is the representative browse product RGB(s) (see Table 2 for abbreviations) for that class set.
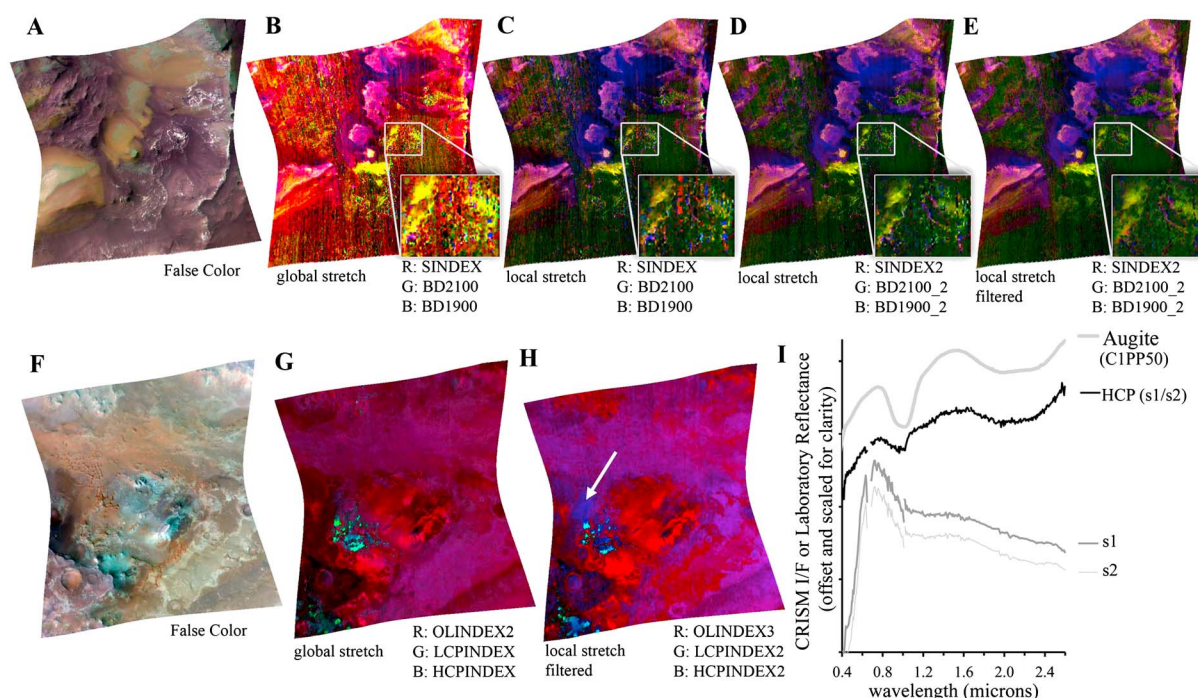
Figure 10. A detailed example of summary and browse product development. The top row shows (a) CRISM MTRDR scene FRT0000B385 in false color stepped through (b) the old HYD browse product with a "global" stretch applied, (c) the same HYD product with the new "local" stretch applied, (d) the new parameter formulations for the revised HYD product, and (e) the new HYD product after noise filtering results. Figures 10b–10e include a zoom-up box of a small region illustrating fine-scale changes that occur with improved stretching logic, refined parameter formulations, and noise filtering. The bottom row shows (f) CRISM MTRDR scene FRT000064D9 in false color stepped through (g) the old MAF browse product with global stretch applied, (h) the new MAF product with local stretch and noise filtering, and (i) extracted and ratioed CRISM I/F spectra from a particular location in this scene (white arrow, Figure 10h) and comparable laboratory spectra (RELAB) of high-Ca pyroxene (HCP) material. The old HCPINDEX displays no detection for this material (Figure 10g, blue channel), whereas the new HCPINDEX2 shows a strong detection of HCP (Figure 10h, blue channel).

particular CRISM observation, and the specific observational conditions under which the individual image was acquired (e.g., level of noise dependent on IR detector temperature and atmospheric opacity). While placing the same stretch limits on every scene for a particular summary product (i.e., a "global" stretch) ensures cross-comparison between scenes and preservation of the data set-wide dynamic range of a summary product, weak but significant detections are frequently lost in a global stretch. Thus, the statistical stretching of summary products must ensure that significant detections are not lost in the final browse product display and that background signal in a summary product is not overstretched.

For summary products R530, R440, R600, R770, R1080, R1506, R2529, R3920, SH600_2, IRA, ISLOPE1, and IRR2, the stretch limits are taken as the 0.1th and 99.9th percentiles of the local histogram (the histogram for the individual scene). To constrain the expected distribution values for the remaining summary products, cumulative statistics were derived for over 100 CRISM images representative of the global parameter distribution. These summary products have a fixed lower stretch limit at a parameter value of 0, usually corresponding with a band depth of zero. The upper stretch limit is either set to the 99th percentile of the cumulative histogram, or the 99.9th percentile of the local histogram, whichever is greater. This ensures that the resulting stretched summary product will not overenhance a small tail of the distribution that may be subject to outliers (unmitigated noise).

6. Summary Product Limitations

While summary products are carefully constructed to avoid false positives from spectrally similar phases and known characteristics of the CRISM data set, the products may be nonunique, providing large values for multiple spectral signatures or for data with unanticipated spectral anomalies. Furthermore, the strength of a particular summary product may not be used to infer quantitative mineral abundance. Although the depth of
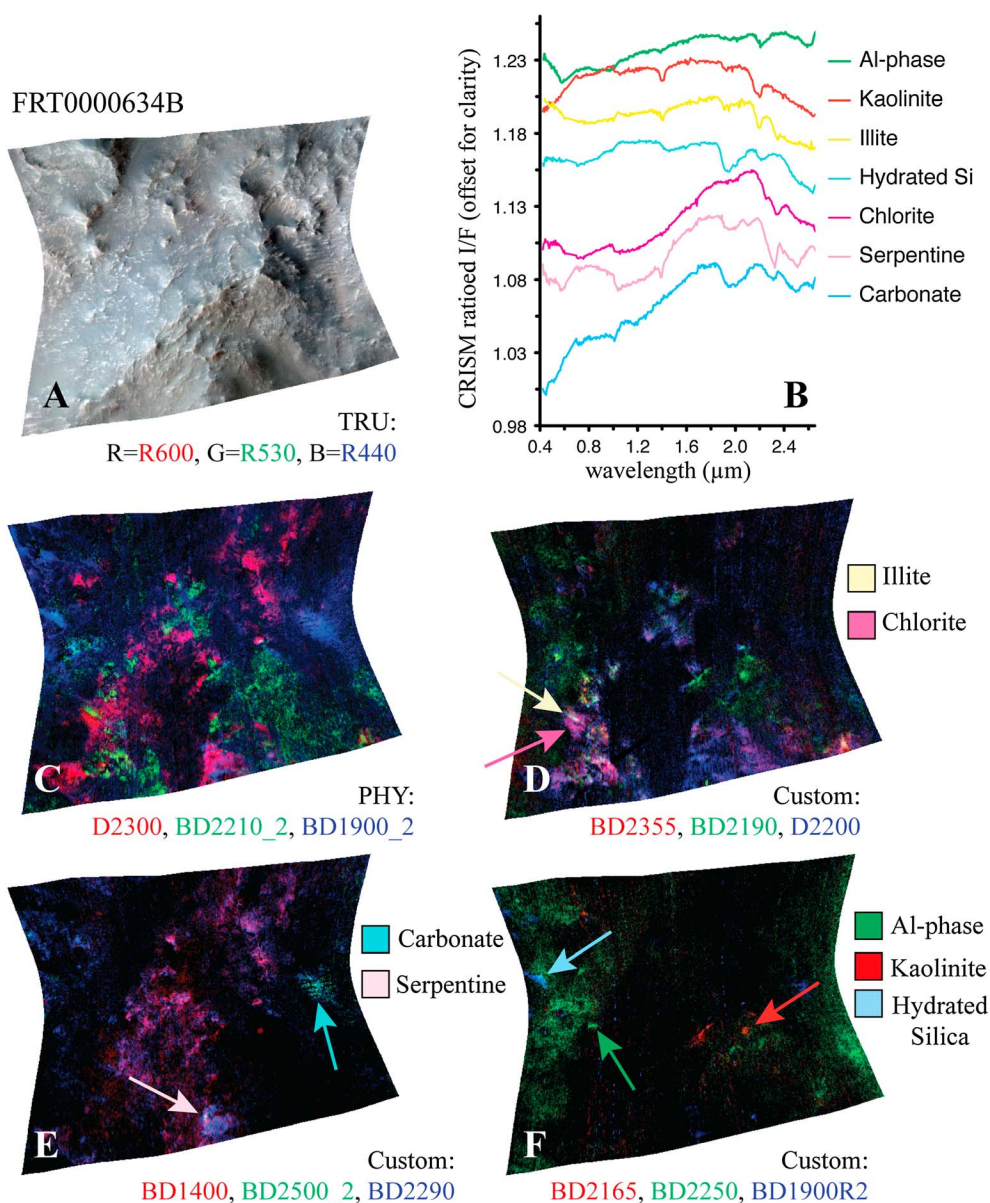
Figure 11. A particularly diverse CRISM scene (FRT0000634B) revealing the utility of new summary product formulations. Although (a) the VNIR color stretch of this scene is somewhat homogenous, there are at least (b) seven type spectra represented in the image (locations of extracted spectra shown in subsequent panels with arrows). While (c) the standard PHY browse product reveals some hydroxylated silicate diversity, (d–f) custom combinations of new summary products are able to visually distinguish subtle spectral differences in the scene.

an absorption feature that is associated with a particular mineral typically scales with that mineral's abundance, the particle size, albedo, and mixtures with other minerals obscure this relationship [e.g., *Clark and Roush*, 1984]. In all cases, detailed analysis of CRISM spectra must be used to match absorption band positions and relative strength for positive mineral identification. Figure 9 provides a visual representation of the sensitivity of the majority of the summary products to different minerals, where each formulation has been applied to both the laboratory and MICA spectra presented in this work. The similarity in overall response to the two data sets suggests that the products are robust against observational factors specific to the CRISM data set. These matrices also provide guidelines for understanding the sensitivity of the summary products to multiple spectral signatures and the advantage of utilizing the combination of products together to visualize the spectral diversity in a CRISM scene (i.e., browse products).

Importantly, although the summary products serve as mineral indicator maps, precise identification of the presence or absence of phases still requires examination of the spectra themselves. For example, small absorptions diagnostic of prehnite versus chlorite (e.g., the 1.47 μm absorption) are not globally mappable in this parameter set, leaving it to the data user to identify locales of interest, examine CRISM spectral data, and design custom scene-specific maps for making such fine distinctions or employing more advanced heuristic mineral identification protocols [e.g., *Clark et al.*, 2003].

7. Illustrative Examples of Summary Product Revisions and Additions

Figure 10 presents a visual of the refined and enhanced nature of a subset of the new summary products and composite browse products as compared to previous iterations. Examples of the revisions of hydrated or hydroxylated mineral parameters, D2300, BD2210, and BD1900, as well as mafic parameters, OLINDEX2 [*Salvatore et al.*, 2010], LCPINDEX, and HCPINDEX [*Pelkey et al.*, 2007], are shown. Figures 10b–10e illustrate the visual changes associated with the new summary products and the noise filtering results. Revisions to these parameters' formulations and new naming conventions are summarized in Table 2. All parameters have been reformulated to utilize hyperspectral sampling, combining multiple bands through a median filter to calculate the reflectance at a single wavelength (see section 4.4). A slight change has been made to OLINDEX2 (now named OLINDEX3) to utilize more channels between 1080 and 1470 nm. The formulas for the pyroxene indices LCPINDEX and HCPINDEX are substantially altered. The old formulation for these parameters was written to identify convexity at the region between the ~1 and ~2 μm pyroxene absorptions (at 1330 nm for LCP and 1470 nm for HCP). The revised LCPINDEX2 and HCPINDEX2 are sensitive to the broad 2 μm pyroxene absorption and are less subject to false positives from other spectral end-members or mixtures that display convexity between ~1.3 and 1.5 μm. This is illustrated in Figure 10, where an RGB combination of three summary products is displayed for both the original (Figure 10g) and revised (Figure 10h) parameters. Extracted spectra (Figure 10i) demonstrate locations where HCPINDEX2 correctly indicates the presence of high calcium pyroxene, where the original HCPINDEX shows no significant detection. The series of panels in Figure 10 also demonstrate improved statistical stretching logic and noise filtering procedures described in section 5.

Furthermore, additional summary products introduced in this work (e.g., BD2165, BD2190, MIN2200, and MIN2250) allow for discrimination of subtle spectral differences in a CRISM scene. These summary products may be used in custom combinations not provided by the standard browse product set (Table 2) to highlight the particular phases that are present in a scene. The spectral end-members of a compositionally diverse scene in Claritas Rise are shown in Figure 11 to demonstrate the utility of custom combinations. While the standard PHY browse product (Figure 11c) does reveal that there are likely both Al- and Fe/Mg-hydroxylated phases in the scene, it provides no further discrimination of these phases. A combination of summary products tuned to absorption features at 2.2 and 2.35 μm can differentiate between chlorite and illite (Figure 11d), while products used to highlight 2.3 and 2.5 μm absorptions emphasize carbonate and serpentine (Figure 11e). Several of the new summary products around 2.2 μm may be combined to differentiate between kaolinite, Al smectites, and hydrated silica (Figure 11f). While it is impractical to provide examples for each revised or additional summary product, the "Rationale" and "Caveats" information provided in Table 1, as well as the "Significance and Interpretation" provided in Table 2 provides guidelines for analyzing the standard browse products and creating custom summary product combinations to assist with detailed analysis.

8. Conclusions

Because the original CRISM summary products were based on a priori expectations of surface compositions from OMEGA data, new summary products are needed to reflect the increasingly complex diversity of minerals on the surface. The expanded parameter set exploits the hyperspectral characteristics of the CRISM-targeted observation data set and provides a more robust and comprehensive set of parameters. Because the revised summary products are tailored to the currently known suite of minerals, they are more representative of the diversity of the surface than the original set. The revised summary products will be delivered to the PDS with the new MTRDR product data set and integrated into a forthcoming release of the CAT. These products will provide a useful tool for advancing scientific interpretation and assessment of future candidate landing sites for in situ investigations.

References

Arvidson, R. E., F. Poulet, J.-P. Bibring, M. Wolff, A. Gendrin, R. V. Morris, J. J. Freeman, Y. Langevin, N. Mangold, and G. Bellucci (2005), Spectral reflectance and morphologic correlations in eastern Terra Meridiani, Mars, *Science*, *307*(5715), 1591–1594, doi:10.1126/science.1109509. [Available at http://www.sciencemag.org/content/307/5715/1591.full.], Accessed 20 January 2014.

Bandfield, J. L. (2002), Global mineral distributions on Mars, *J. Geophys. Res.*, *107*(E6, 5042), doi:10.1029/2001JE001510.

Bandfield, J. L., V. E. Hamilton, and P. R. Christensen (2000), A global view of Martian surface compositions from MGS-TES, *Science*, *287*(5458), 1626–1630.

Bell, J. F., P. G. Lucey, and T. B. McCord (1992), Charge-coupled device imaging spectroscopy of Mars. 1. Instrumentation and data reduction/ analysis procedures, *Exp. Astron.*, *2*(5), 287–306, doi:10.1007/BF00690087. [Available at http://link.springer.com/10.1007/BF00690087.], Accessed 5 December 2013.

Bell, J. F., et al. (2000), Mineralogic and compositional properties of Martian soil and dust: Results from Mars Pathfinder, *J. Geophys. Res.*, *105*(E1), 1721–1755, doi:10.1029/1999JE001060.

Bibring, J.-P., et al. (1989), Results from the ISM experiment, *Nature*, *341*(6243), 591–593, doi:10.1038/341591a0. [Available at 10.1038/341591a0.], Accessed 20 January 2014.

Bibring, J.-P., et al. (2004), OMEGA: Observatoire pour la Minéralogie, l'Eau, les Glaces et l'Activité, in *Mars Express: The Scientific Payload*, vol. 1240, Eur. Space Agency Spec. Publ. (ESA-SP), edited by A. Wilson and A. Chicarro, pp. 37–49.

Bishop, J. L., et al. (2008), Phyllosilicate diversity and past aqueous activity revealed at Mawrth Vallis, Mars, *Science*, *321*(5890), 830–833, doi:10.1126/science.1159699. [Available at http://www.sciencemag.org/content/321/5890/830.abstract.], Accessed 18 November 2013.

Bishop, J. L., et al. (2009), Mineralogy of Juventae Chasma: Sulfates in the light-toned mounds, mafic minerals in the bedrock, and hydrated silica and hydroxylated ferric sulfate on the plateau, *J. Geophys. Res.*, *114*, E00D09, doi:10.1029/2009JE003352.

Bishop, J. L., et al. (2013), Mineralogy and morphology of geologic units at Libya Montes, Mars: Ancient aqueously derived outcrops, mafic flows, fluvial features, and impacts, *J. Geophys. Res. Planets*, *118*, 487–513, doi:10.1029/2012JE004151.

Breuer, D. (2003), Early plate tectonics versus single-plate tectonics on Mars: Evidence from magnetic field history and crust evolution, *J. Geophys. Res.*, *108*(E7), 5072, doi:10.1029/2002JE001999.

Bristow, T. F., and R. E. Milliken (2011), Terrestrial perspective on authigenic clay mineral production in ancient Martian lakes, *Clays Clay Miner.*, *59*(4), 339–358, doi:10.1346/CCMN.2011.0590401. [Available at http://openurl.ingenta.com/content/xref?genre=article&issn=0009-8604&volume=59&issue=4&spage=339.], Accessed 10 February 2014.

Brown, A. J., W. M. Calvin, P. C. McGuire, and S. L. Murchie (2010), Compact Reconnaissance Imaging Spectrometer for Mars (CRISM) south polar mapping: First Mars year of observations, *J. Geophys. Res.*, *115*, E00D13, doi:10.1029/2009JE003333.

Burns, R. G. (1993), *Mineralogical Applications of Crystal Field Theory*, Cambridge Univ. Press, New York.

Calvin, W. M., L. H. Roach, F. P. Seelos, K. D. Seelos, R. O. Green, S. L. Murchie, and J. F. Mustard (2009), Compact Reconnaissance Imaging Spectrometer for Mars observations of northern Martian latitudes in summer, *J. Geophys. Res.*, *114*, E00D11, doi:10.1029/2009JE003348.

Carter, J., and F. Poulet (2013), Ancient plutonic processes on Mars inferred from the detection of possible anorthositic terrains, *Nat. Geosci.*, *6*(12), 1008–1012, doi:10.1038/ngeo1995. [Available at 10.1038/ngeo1995.], Accessed 18 November 2013.

Carter, J., F. Poulet, S. Murchie, and J. P. Bibring (2013a), Automated processing of planetary hyperspectral datasets for the extraction of weak mineral signatures and applications to CRISM observations of hydrated silicates on Mars, *Planet. Space Sci.*, *76*, 53–67. [Available at http://www.sciencedirect.com/science/article/pii/S0032063312003625.], Accessed 22 November 2013.

Carter, J., F. Poulet, J.-P. Bibring, N. Mangold, and S. Murchie (2013b), Hydrous minerals on Mars as seen by the CRISM and OMEGA imaging spectrometers: Updated global view, *J. Geophys. Res. Planets*, *118*, 831–858, doi:10.1029/2012JE004145.

Catling, D. C. (1999), A chemical model for evaporites on early Mars: Possible sedimentary tracers of the early climate and implications for exploration, *J. Geophys. Res.*, *104*(E7), 16,453–16,469, doi:10.1029/1998JE001020.

Cheek, L. C., K. L. Donaldson Hanna, C. M. Pieters, J. W. Head, and J. L. Whitten (2013), The distribution and purity of anorthosite across the Orientale basin: New perspectives from Moon Mineralogy Mapper data, *J. Geophys. Res. Planets*, *118*, 1805–1820, doi:10.1002/jgre.20126.

Chipera, S. J., and D. T. Vaniman (2007), Experimental stability of magnesium sulfate hydrates that may be present on Mars, *Geochim. Cosmochim. Acta*, *71*(1), 241–250, doi:10.1016/j.gca.2006.07.044. [Available at http://www.sciencedirect.com/science/article/pii/S0016703706020965.], Accessed 10 February 2014.

Christensen, P. R., et al. (2001), Mars Global Surveyor Thermal Emission Spectrometer experiment: Investigation description and surface science results, *J. Geophys. Res.*, *106*(E10), 23,823–23,871.

Clark, R. N., and T. L. Roush (1984), Reflectance spectroscopy: Quantitative analysis techniques for remote sensing applications, *J. Geophys. Res.*, *89*(B7), 6329, doi:10.1029/JB089iB07p06329.

Clark, R. N., T. V. V. King, M. Klejwa, G. A. Swayze, and N. Vergo (1990), High spectral resolution reflectance spectroscopy of minerals, *J. Geophys. Res.*, *95*(B8), 12,653–12,680, doi:10.1029/JB095iB08p12653.

Clark, R. N., G. A. Swayze, K. E. Livo, R. F. Kokaly, S. J. Sutley, J. B. Dalton, R. R. McDougal, and C. A. Gent (2003), Imaging spectroscopy: Earth and planetary remote sensing with the USGS Tetracorder and expert systems, *J. Geophys. Res.*, *108*(E12), 5131, doi:10.1029/2002JE001847.

Cloutis, E. A. (2002), Spectral reflectance properties of zeolites and remote sensing implications, *J. Geophys. Res.*, *107*(E9), 5067, doi:10.1029/2000JE001467.

Cloutis, E. A., et al. (2006), Detection and discrimination of sulfate minerals using reflectance spectroscopy, *Icarus*, *184*(1), 121–157. [Available at http://www.sciencedirect.com/science/article/pii/S0019103506001242.], Accessed 5 December 2013.

Cull, S., R. E. Arvidson, M. Mellon, S. Wiseman, R. Clark, T. Titus, R. V. Morris, and P. McGuire (2010), Seasonal H_2O and CO_2 ice cycles at the Mars Phoenix landing site: 1. Prelanding CRISM and HiRISE observations, *J. Geophys. Res.*, *115*, E00D16, doi:10.1029/2009JE003340.

Dalton, J. B., D. J. Bove, C. S. Mladinich, and B. W. Rockwell (2004), Identification of spectrally similar materials using the USGS Tetracorder algorithm: The calcite–epidote–chlorite problem, *Remote Sens. Environ.*, *89*(4), 455–466, doi:10.1016/j.rse.2003.11.011. [Available at http://www.sciencedirect.com/science/article/pii/S0034425703003389.], Accessed 18 February 2014.

Edwards, C. S., P. R. Christensen, and V. E. Hamilton (2008), Evidence for extensive olivine-rich basalt bedrock outcrops in Ganges and Eos chasmas, Mars, *J. Geophys. Res.*, *113*, E11003, doi:10.1029/2008JE003091.

Ehlmann, B. L., and C. S. Edwards (2014), Mineralogy of the Martian surface, *Annu. Rev. Earth Planet. Sci.*, *42*, doi:10.1146/annurev-earth-060313-055024. [Available at http://www.annualreviews.org/doi/abs/10.1146/annurev-earth-060313-055024.], Accessed 14 January 2014.

Ehlmann, B. L., J. F. Mustard, S. L. Murchie, F. Poulet, J. L. Bishop, L. H. Roach, T. L. Roush, G. A. Swayze, and J. J. Wray (2008), Orbital identification of carbonate-bearing rocks on Mars, *Science*, *322*, 1828–1832.

Ehlmann, B. L., et al. (2009), Identification of hydrated silicate minerals on Mars using MRO-CRISM: Geologic context near Nili Fossae and implications for aqueous alteration, *J. Geophys. Res.*, *114*, E00D08, doi:10.1029/2009JE003339.

Ehlmann, B. L., J. F. Mustard, and S. L. Murchie (2010), Geologic setting of serpentine deposits on Mars, *Geophys. Res. Lett.*, *37*, L06201, doi:10.1029/2010GL042596.

Ehlmann, B. L., J. F. Mustard, R. N. Clark, G. A. Swayze, and S. L. Murchie (2011a), Evidence for low-grade metamorphism, hydrothermal alteration, and diagenesis on Mars from phyllosilicate mineral assemblages, *Clays Clay Miner.*, *59*(4), 359–377, doi:10.1346/CCMN.2011.0590402. [Available at http://openurl.ingenta.com/content/xref?genre=article&issn=0009-8604&volume=59&issue=4&spage=359.], Accessed 20 November 2013.

Ehlmann, B. L., J. F. Mustard, S. L. Murchie, J.-P. Bibring, A. Meunier, A. A. Fraeman, and Y. Langevin (2011b), Subsurface water and clay mineral formation during the early history of Mars, *Nature*, *479*(7371), 53–60, doi:10.1038/nature10582. [Available at http://www.ncbi.nlm.nih.gov/pubmed/22051674.], Accessed 20 November 2013.

Eugster, H. P. (1980), Geochemistry of evaporitic lacustrine deposits, *Annu. Rev. Earth Planet. Sci.*, *8*(1), 35–63, doi:10.1146/annurev.ea.08.050180.000343. [Available at http://www.annualreviews.org/doi/abs/10.1146/annurev.ea.08.050180.000343.], Accessed 18 February 2014.

Farrand, W. H., J. F. Bell, J. R. Johnson, S. W. Squyres, J. Soderblom, and D. W. Ming (2006), Spectral variability among rocks in visible and near-infrared multispectral Pancam data collected at Gusev crater: Examinations using spectral mixture analysis and related techniques, *J. Geophys. Res.*, *111*, E02S15, doi:10.1029/2005JE002495.

Farrand, W. H., T. D. Glotch, J. W. Rice, J. A. Hurowitz, and G. A. Swayze (2009), Discovery of jarosite within the Mawrth Vallis region of Mars: Implications for the geologic history of the region, *Icarus*, *204*(2), 478–488, doi:10.1016/j.icarus.2009.07.014. [Available at http://linkinghub.elsevier.com/retrieve/pii/S0019103509002929.], Accessed 19 November 2013.

Fink, U., and G. T. Sill (1982), The infrared spectral properties of frozen volatiles, in *Comets. (A83-13376 03-90)*, pp. 164–202. [Available at http://adsabs.harvard.edu/abs/1982come.coll..164F.], Accessed 7 February 2014, Univ. of Arizona Press, Tucson, Ariz.

Fischer, E., and C. Pieters (1993), The Continuum Slope of Mars: Bidirectional reflectance investigations and applications to Olympus Mons, Icarus, *102*(2), 185–202.

Flahaut, J., J. F. Mustard, C. Quantin, H. Clenet, P. Allemand, and P. Thomas (2011), Dikes of distinct composition intruded into Noachian-aged crust exposed in the walls of Valles Marineris, *Geophys. Res. Lett.*, *38*, L15202, doi:10.1029/2011GL048109.

Gaffey, S. J. (1987), Spectral reflectance of carbonate minerals in the visible and near infrared (0.35–2.55 um): Anhydrous carbonate minerals, *J. Geophys. Res.*, *92*(B2), 1429–1440, doi:10.1029/JB092iB02p01429.

Gendrin, A., et al. (2005), Sulfates in Martian layered terrains: The OMEGA/Mars Express view, *Science*, *307*(5715), 1587–1591, doi:10.1126/science.1109087. [Available at http://www.sciencemag.org/content/307/5715/1587.full.], Accessed 29 November 2013.

Glotch, T. D., J. L. Bandfield, L. L. Tornabene, H. B. Jensen, and F. P. Seelos (2010), Distribution and formation of chlorides and phyllosilicates in Terra Sirenum, Mars, *Geophys. Res. Lett.*, *37*, 1–5, doi:10.1029/2010GL044557.

Hansen, G. B. (1997), Spectral absorption of solid CO_2 from the ultraviolet to the far-infrared, *Adv. Sp. Res.*, *20*(8), 1613–1616. [Available at http://www.sciencedirect.com/science/article/pii/S027311779700820X.], Accessed 4 December 2013.

Hoefen, T. M., R. N. Clark, J. L. Bandfield, M. D. Smith, J. C. Pearl, and P. R. Christensen (2003), Discovery of olivine in the Nili Fssae region of Mars, *Science*, *302*(5645), 627–630, doi:10.1126/science.1089647. [Available at http://www.ncbi.nlm.nih.gov/pubmed/14576430.], Accessed 20 November 2013.

Huang, J., C. S. Edwards, B. H. N. Horgan, P. R. Christensen, M. D. Kraft, and L. Xiao (2012), Identification and mapping of dikes with relatively primitive compositions in Thaumasia Planum on Mars: Implications for Tharsis volcanism and the opening of Valles Marineris, *Geophys. Res. Lett.*, *39*, L17201, doi:10.1029/2012GL052523.

King, T. V. V., and R. N. Clark (1989), Spectral characteristics of chlorites and Mg-serpentines using high-resolution reflectance spectroscopy, *J. Geophys. Res.*, *94*(B10), 13997, doi:10.1029/JB094iB10p13997.

King, T. V. V., and W. I. Ridley (1987), Relation of the spectroscopic reflectance of olivine to mineral chemistry and some remote sensing implications, *J. Geophys. Res.*, *92*(B11), 11457, doi:10.1029/JB092iB11p11457.

Koeppen, W. C., and V. E. Hamilton (2008), Global distribution, composition, and abundance of olivine on the surface of Mars from thermal infrared data, *J. Geophys. Res.*, (113), E05001, doi:10.1029/2007JE002984.

Langevin, Y., F. Poulet, J.-P. Bibring, and B. Gondet (2005), Sulfates in the north polar region of Mars detected by OMEGA/Mars Express, *Science*, *307*(5715), 1584–1586, doi:10.1126/science.1109091. [Available at http://www.sciencemag.org/content/307/5715/1584.], Accessed 20 January 2014.

Langevin, Y., J.-P. Bibring, F. Montmessin, F. Forget, M. Vincendon, S. Douté, F. Poulet, and B. Gondet (2007), Observations of the south seasonal cap of Mars during recession in 2004–2006 by the OMEGA visible/near-infrared imaging spectrometer on board Mars Express, *J. Geophys. Res.*, *112*, E08S12, doi:10.1029/2006JE002841.

Le Deit, L., O. Bourgeois, D. Mège, E. Hauber, S. Le Mouélic, M. Massé, R. Jaumann, and J.-P. Bibring (2010), Morphology, stratigraphy, and mineralogical composition of a layered formation covering the plateaus around Valles Marineris, Mars: Implications for its geological history, *Icarus*, *208*(2), 684–703. [Available at http://www.sciencedirect.com/science/article/pii/S0019103510001144.], Accessed 5 December 2013.

Le Deit, L., J. Flahaut, C. Quantin, E. Hauber, D. Mège, O. Bourgeois, J. Gurgurewicz, M. Massé, and R. Jaumann (2012), Extensive surface pedogenic alteration of the Martian Noachian crust suggested by plateau phyllosilicates around Valles Marineris, *J. Geophys. Res.*, *117*, E00J05, doi:10.1029/2011JE003983.

Lichtenberg, K. A., et al. (2010), Stratigraphy of hydrated sulfates in the sedimentary deposits of Aram Chaos, Mars, *J. Geophys. Res.*, *115*, E00D17, doi:10.1029/2009JE003353.

Marzo, G. A., A. F. Davila, L. L. Tornabene, J. M. Dohm, A. G. Fairén, C. Gross, T. Kneissl, J. L. Bishop, T. L. Roush, and C. P. McKay (2010), Evidence for Hesperian impact-induced hydrothermalism on Mars, *Icarus*, *208*(2), 667–683. [Available at http://www.sciencedirect.com/science/article/pii/S0019103510001156.], Accessed 5 December 2013.

Massé, M., O. Bourgeois, S. Le Mouélic, C. Verpoorter, L. Le Deit, and J. P. Bibring (2010), Martian polar and circum-polar sulfate-bearing deposits: Sublimation tills derived from the North Polar Cap, *Icarus*, *209*(2), 434–451. [Available at http://www.sciencedirect.com/science/article/pii/S0019103510001740.], Accessed 5 December 2013.

Massé, M., O. Bourgeois, S. Le Mouélic, C. Verpoorter, A. Spiga, and L. Le Deit (2012), Wide distribution and glacial origin of polar gypsum on Mars. [Available at http://www.sciencedirect.com/science/article/pii/S0012821X11007035.], Accessed 5 December 2013.

McGuire, P. C., et al. (2009), An improvement to the volcano-scan algorithm for atmospheric correction of CRISM and OMEGA spectral data, *Planet. Space Sci.*, *57*(7), 809–815, doi:10.1016/j.pss.2009.03.007. [Available at http://adsabs.harvard.edu/abs/2009P%26SS...57..809M.], Accessed 20 January 2014.

Michalski, J. R., and P. B. Niles (2010), Deep crustal carbonate rocks exposed by meteor impact on Mars, *Nat. Geosci.*, *3*(11), 751–755, doi:10.1038/ngeo971. [Available at 10.1038/ngeo971.], Accessed 6 December 2013.

Milam, K. A., H. Y. McSween, J. Moersch, and P. R. Christensen (2010), Distribution and variation of plagioclase compositions on Mars, *J. Geophys. Res.*, *115*, E09004, doi:10.1029/2009JE003495.

Milliken, R. E., and D. L. Bish (2010), Sources and sinks of clay minerals on Mars, *Philos. Mag.*, *90*(17–18), 2293–2308, doi:10.1080/14786430903575132. [Available at http://www.tandfonline.com/doi/abs/10.1080/14786430903575132.], Accessed 10 February 2014.

Milliken, R. E., et al. (2008), Opaline silica in young deposits on Mars, *Geology*, *36*(11), 847–850, doi:10.1130/G24967A.1. [Available at http://geology.gsapubs.org/cgi/doi/10.1130/G24967A.1.], Accessed 20 November 2013.

Morgan, F., J. F. Mustard, S. M. Wiseman, F. P. Seelos, S. L. Murchie, P. C. McGuire, and C. Team (2011), Improved algorithm for CRISM volcano scan atmospheric correction, *Lunar Planet. Inst. Sci. Conf. Abstr.*, *42*, 2453. [Available at http://adsabs.harvard.edu/abs/2011LPI....42.2453M.], Accessed 20 November 2013.

Morris, R. V., et al. (2000), Mineralogy, composition, and alteration of Mars Pathfinder rocks and soils: Evidence from multispectral, elemental, and magnetic data on terrestrial analogue, SNC meteorite, and Pathfinder samples, *J. Geophys. Res.*, *105*(E1), 1757–1817, doi:10.1029/1999JE001059.

Murchie, S. L., et al. (2009), A synthesis of Martian aqueous mineralogy after 1 Mars year of observations from the Mars Reconnaissance Orbiter, *J. Geophys. Res.*, *114*, E00D06, doi:10.1029/2009JE003342.

Murchie, S., et al. (2007), Compact Reconnaissance Imaging Spectrometer for Mars (CRISM) on Mars Reconnaissance Orbiter (MRO), *J. Geophys. Res.*, *112*, E05S03, doi:10.1029/2006JE002682.

Mustard, J. F., F. Poulet, A. Gendrin, J.-P. Bibring, Y. Langevin, B. Gondet, N. Mangold, G. Bellucci, and F. Altieri (2005), Olivine and pyroxene diversity in the crust of Mars, *Science*, *307*(5715), 1594–1597, doi:10.1126/science.1109098. [Available at http://www.ncbi.nlm.nih.gov/pubmed/15718427.], Accessed 22 November 2013.

Mustard, J. F., et al. (2008), Hydrated silicate minerals on Mars observed by the Mars Reconnaissance Orbiter CRISM instrument, *Nature*, *454*(7202), 305–309, doi:10.1038/nature07097. [Available at http://www.ncbi.nlm.nih.gov/pubmed/18633411.], Accessed 11 November 2013.

Mustard, J. F., B. L. Ehlmann, S. L. Murchie, F. Poulet, N. Mangold, J. W. Head, J.-P. Bibring, and L. H. Roach (2009), Composition, morphology, and stratigraphy of noachian crust around the Isidis basin, *J. Geophys. Res.*, *114*, E00D12, doi:10.1029/2009JE003349.

Noe Dobrea, E. Z., J. Moore, A. Howard, D. Catling, and J. Grant (2008), Spectral and geomorphic evidence for a past inland sea in Eridania Basin, Mars, *Am. Geophys. Union*. [Available at http://adsabs.harvard.edu/abs/2008AGUFM.P32B..03N.], Accessed 20 May 2014.

Ody, A., F. Poulet, J.-P. Bibring, D. Loizeau, J. Carter, B. Gondet, and Y. Langevin (2013), Global investigation of olivine on Mars: Insights into crust and mantle compositions, *J. Geophys. Res. Planets*, *118*, 234–262, doi:10.1029/2012JE004149.

Ohtake, M., et al. (2009), The global distribution of pure anorthosite on the Moon, *Nature*, *461*(7261), 236–240, doi:10.1038/nature08317. [Available at 10.1038/nature08317.], Accessed 9 November 2013.

Osterloo, M. M., V. E. Hamilton, J. L. Bandfield, T. D. Glotch, A. M. Baldridge, P. R. Christensen, L. L. Tornabene, and F. S. Anderson (2008), Chloride-bearing materials in the southern highlands of Mars, *Science*, *319*(5870), 1651–1654, doi:10.1126/science.1150690. [Available at http://www.sciencemag.org/content/319/5870/1651.abstract.], Accessed 6 December 2013.

Pan, L., and B. L. Ehlmann (2014), Possible formation mechanisms of phyllosilicates and hydrated silica in Acidalia Planitia, *45th Lunar Planet. Sci. Conf.*, #1245.

Pelkey, S. M., et al. (2007), CRISM multispectral summary products: Parameterizing mineral diversity on Mars from reflectance, *J. Geophys. Res.*, *112*, E08S14, doi:10.1029/2006JE002831.

Pollack, J. B., J. F. Kasting, S. M. Richardson, and K. Poliakoff (1987), The case for a wet, warm climate on early Mars, *Icarus*, *71*, 203–24. [Available at http://www.ncbi.nlm.nih.gov/pubmed/11539035.], Accessed 11 February 2014.

Poulet, F., C. Gomez, J.-P. Bibring, Y. Langevin, B. Gondet, P. Pinet, G. Belluci, and J. Mustard (2007), Martian surface mineralogy from Observatoire pour la Minéralogie, l'Eau, les Glaces et l'Activité on board the Mars Express spacecraft (OMEGA/MEx): Global mineral maps, *J. Geophys. Res.*, *112*, E08S02, doi:10.1029/2006JE002840.

Rice, M. S., E. A. Cloutis, J. F. Bell, D. L. Bish, B. H. Horgan, S. A. Mertzman, M. A. Craig, R. W. Renaut, B. Gautason, and B. Mountain (2013), Reflectance spectra diversity of silica-rich materials: Sensitivity to environment and implications for detections on Mars, *Icarus*, *223*(1), 499–533, doi:10.1016/j.icarus.2012.09.021. [Available at http://www.sciencedirect.com/science/article/pii/S0019103512003946.], Accessed 11 February 2014.

Roach, L. H., J. F. Mustard, S. L. Murchie, J.-P. Bibring, F. Forget, K. W. Lewis, O. Aharonson, M. Vincendon, and J. L. Bishop (2009), Testing evidence of recent hydration state change in sulfates on Mars, *J. Geophys. Res.*, *114*, E00D02, doi:10.1029/2008JE003245.

Roach, L. H., J. F. Mustard, M. D. Lane, J. L. Bishop, and S. L. Murchie (2010a), Diagenetic haematite and sulfate assemblages in Valles Marineris, *Icarus*, *207*(2), 659–674. [Available at http://www.sciencedirect.com/science/article/pii/S0019103509004758.], Accessed 20 November 2013.

Roach, L. H., J. F. Mustard, G. Swayze, R. E. Milliken, J. L. Bishop, S. L. Murchie, and K. Lichtenberg (2010b), Hydrated mineral stratigraphy of Ius Chasma, Valles Marineris, *Icarus*, *206*(1), 253–268, doi:10.1016/j.icarus.2009.09.003. [Available at http://linkinghub.elsevier.com/retrieve/pii/S0019103509003844.], Accessed 20 November 2013.

Rogers, A. D., and R. L. Fergason (2011), Regional-scale stratigraphy of surface units in Tyrrhena and Iapygia Terrae, Mars: Insights into highland crustal evolution and alteration history, *J. Geophys. Res.*, *116*, E08005, doi:10.1029/2010JE003772.

Ruff, S. W. (2004), Spectral evidence for zeolite in the dust on Mars, *Icarus*, *168*(1), 131–143, doi:10.1016/j.icarus.2003.11.003. [Available at http://www.sciencedirect.com/science/article/pii/S0019103503003865.], Accessed 18 February 2014.

Salvatore, M. R., J. F. Mustard, M. B. Wyatt, and S. L. Murchie (2010), Definitive evidence of Hesperian basalt in Acidalia and Chryse planitiae, *J. Geophys. Res.*, *115*, E07005, doi:10.1029/2009JE003519.

Schiffman, P., and H. W. Day (1999), Petrological methods for the study of very low-grade metabasites, in *Low-Grade Metamorphism*, edited by M. Frey and D. Robinson, pp. 108–142, Blackwell Publishing Ltd., Oxford, U. K. [Available at http://doi.wiley.com/10.1002/9781444313345.], Accessed 10 February 2014.

Schubert, G., D. L. Turcotte, and P. Olson (2001), *Mantle Convection in the Earth and Planets*, Cambridge Univ. Press, New York. [Available at http://www.amazon.com/Mantle-Convection-Earth-Planets-Volume/dp/0521798361.], Accessed 18 February 2014.

Seelos, F. P., et al. (2009), CRISM hyperspectral data filtering with application to MSL landing site selection, *AGU Fall Meet. Abstr.*, A1234. [Available at http://adsabs.harvard.edu/abs/2009AGUFM.P23A1234S.], Accessed 20 November 2013.

Seelos, F. P., S. L. Murchie, D. C. Humm, O. S. Barnouin, F. Morgan, H. W. Taylor, C. Hash, and C. Team (2011), CRISM data processing and analysis products update — Calibration, correction, and visualization, *Lunar Planet. Inst. Sci. Conf. Abstr.*, *42*, 1438. [Available at http://adsabs.harvard.edu/abs/2011LPI....42.1438S.], Accessed 20 November 2013.

Seelos, F. P., M. F. Morgan, H. W. Taylor, S. L. Murchie, D. C. Humm, K. D. Seelos, O. S. Barnouin, C. E. Viviano, and C. R. I. S. M. Team (2012), CRISM Map Projected Targeted Reduced Data Records (MTRDRs) – High level analysis and visualization data products, in *Planetary Data: A Workshop for Users and Software Developers*, U.S. Geological Survey, Reston, Va.

Serventi, G., C. Carli, M. Sgavetti, M. Ciarniello, F. Capaccioni, and G. Pedrazzi (2013), Spectral variability of plagioclase–mafic mixtures (1): Effects of chemistry and modal abundance in reflectance spectra of rocks and mineral mixtures, *Icarus*, *226*(1), 282–298. [Available at http://www.sciencedirect.com/science/article/pii/S0019103513002418.], Accessed 5 December 2013.

Sheppard, R. A., and R. L. Hay (2001), Formation of zeolites in open hydrologic systems, *Rev. Mineral. Geochemistry*, *45*(1), 261–275, doi:10.2138/rmg.2001.45.8. [Available at http://rimg.geoscienceworld.org/content/45/1/261.extract.], Accessed 18 February 2014.

Skok, J. R., J. F. Mustard, B. L. Ehlmann, R. E. Milliken, and S. L. Murchie (2010a), Silica deposits in the Nili Patera caldera on the Syrtis Major volcanic complex on Mars, *Nat. Geosci.*, *3*(12), 838–841, doi:10.1038/ngeo990. [Available at 10.1038/ngeo990.], Accessed 5 December 2013.

Skok, J. R., J. F. Mustard, S. L. Murchie, M. B. Wyatt, and B. L. Ehlmann (2010b), Spectrally distinct ejecta in Syrtis Major, Mars: Evidence for environmental change at the Hesperian-Amazonian boundary, *J. Geophys. Res.*, *115*, E00D14, doi:10.1029/2009JE003338.

Skok, J. R., J. F. Mustard, L. L. Tornabene, C. Pan, D. Rogers, and S. L. Murchie (2012), A spectroscopic analysis of Martian crater central peaks: Formation of the ancient crust, *J. Geophys. Res.*, *117*, E00J18, doi:10.1029/2012JE004148.

Smith, M. R., and J. L. Bandfield (2012), Geology of quartz and hydrated silica-bearing deposits near Antoniadi Crater, Mars, *J. Geophys. Res.*, *117*, E06007, doi:10.1029/2011JE004038.

Smith, M. R., J. L. Bandfield, E. A. Cloutis, and M. S. Rice (2013), Hydrated silica on Mars: Combined analysis with near-infrared and thermal-infrared spectroscopy, *Icarus*, *223*(2), 633–648. [Available at http://www.sciencedirect.com/science/article/pii/S0019103513000390.], Accessed 5 December 2013.

Stolper, E. (1982), Water in silicate glasses: An infrared spectroscopic study, *Contrib. to Mineral. Petrol.*, *81*(1), 1–17, doi:10.1007/BF00371154. [Available at http://link.springer.com/10.1007/BF00371154.], Accessed 5 December 2013.

Swayze, G. A., et al. (2008), Discovery of the acid-sulfate mineral alunite in Terra Sirenum, Mars, using MRO CRISM: Possible evidence for acid-saline lacustrine deposits?, *Am*. *Geophys*. *Union*. [Available at http://adsabs.harvard.edu/abs/2008AGUFM.P44A..04S.], Accessed 5 December 2013.

Tornabene, L. L., J. E. Moersch, H. Y. McSween, V. E. Hamilton, J. L. Piatek, and P. R. Christensen (2008), Surface and crater-exposed lithologic units of the Isidis Basin as mapped by coanalysis of THEMIS and TES derived data products, *J. Geophys. Res.*, *113*, E10001, doi:10.1029/2007JE002988.

Viviano, C. E., J. E. Moersch, and H. Y. McSween (2013a), Implications for early hydrothermal environments on Mars through the spectral evidence for carbonation and chloritization reactions in the Nili Fossae region, *J. Geophys. Res. Planets*, *118*, 1858–1872, doi:10.1002/jgre.20141.

Viviano, C. E., S. L. Murchie, J. R. Johnson, and F. P. Seelos (2013b), The distribution and mineralogy of hydrated minerals in wall and floor material of Valles Marineris, *Lunar Planet. Inst. Sci. Conf. Abstr.*, *44*, 2909. [Available at http://adsabs.harvard.edu/abs/2013LPI....44.2909V.], Accessed 22 November 2013.

Wang, A., J. J. Freeman, and B. L. Jolliff (2009), Phase transition pathways of the hydrates of magnesium sulfate in the temperature range 50°C to 5°C: Implication for sulfates on Mars, *J. Geophys. Res.*, *114*, E04010, doi:10.1029/2008JE003266.

Weisenberger, T., and R. S. Selbekk (2008), Multi-stage zeolite facies mineralization in the Hvalfjördur area, Iceland, *Int. J. Earth Sci.*, *98*(5), 985–999, doi:10.1007/s00531-007-0296-6. [Available at http://adsabs.harvard.edu/abs/2009IJEaS..98..985W.], Accessed 18 February 2014.

Weitz, C. M., J. L. Bishop, P. Thollot, N. Mangold, and L. H. Roach (2011), Diverse mineralogies in two troughs of Noctis Labyrinthus, Mars, *Geology*, *39*(10), 899–902, doi:10.1130/G32045.1. [Available at http://geology.gsapubs.org/content/39/10/899.full.], Accessed 18 November 2013.

Wiseman, S. M., R. E. Arvidson, R. V. Morris, F. Poulet, J. C. Andrews-Hanna, J. L. Bishop, S. L. Murchie, F. P. Seelos, D. Des Marais, and J. L. Griffes (2010), Spectral and stratigraphic mapping of hydrated sulfate and phyllosilicate-bearing deposits in northern Sinus Meridiani, Mars, *J. Geophys. Res.*, *115*, E00D18, doi:10.1029/2009JE003354. [Available at http://doi.wiley.com/10.1029/2009JE003354.], Accessed 14 November 2013.

Wray, J. J., S. L. Murchie, S. W. Squyres, F. P. Seelos, and L. L. Tornabene (2009a), Diverse aqueous environments on ancient Mars revealed in the southern highlands, *Geology*, *37*(11), 1043–1046, doi:10.1130/G30331A.1. [Available at http://geology.gsapubs.org/content/37/11/1043.full.], Accessed 18 February 2014.

Wray, J. J., E. Z. Noe Dobrea, R. E. Arvidson, S. M. Wiseman, S. W. Squyres, A. S. McEwen, J. F. Mustard, and S. L. Murchie (2009b), Phyllosilicates and sulfates at Endeavour Crater, Meridiani Planum, Mars, *Geophys. Res. Lett.*, *36*, L21201, doi:10.1029/2009GL040734.

Wray, J. J., S. W. Squyres, L. H. Roach, J. L. Bishop, J. F. Mustard, and E. Z. Noe Dobrea (2010), Identification of the Ca-sulfate bassanite in Mawrth Vallis, Mars, *Icarus*, *209*(2), 416–421, doi:10.1016/j.icarus.2010.06.001. [Available at http://adsabs.harvard.edu/abs/2010Icar..209..416W.], Accessed 20 November 2013.

Wray, J. J., S. L. Murchie, B. L. Ehlmann, R. E. Milliken, J. L. Bishop, K. D. Seelos, E. Z. Noe Dobrea, J. F. Mustard, and S. W. Squyres (2011a), Orbital evidence for iron or calcium carbonates on Mars, *EPSC-DPS Jt. Meet. 2011*. [Available at http://adsabs.harvard.edu/abs/2011epsc.conf.1719W.], Accessed 22 November 2013.

Wray, J. J., et al. (2011b), Columbus crater and other possible groundwater-fed paleolakes of Terra Sirenum, Mars, *J. Geophys. Res.*, *116*, E01001, doi:10.1029/2010JE003694.

Wray, J. J., S. T. Hansen, J. Dufek, G. A. Swayze, S. L. Murchie, F. P. Seelos, J. R. Skok, R. P. Irwin, and M. S. Ghiorso (2013), Prolonged magmatic activity on Mars inferred from the detection of felsic rocks, *Nat. Geosci.*, *6*(12), 1013–1017, doi:10.1038/ngeo1994. [Available at http://www.nature.com/ngeo/journal/v6/n12/full/ngeo1994.html?WT.ec_id=NGEO-201312.], Accessed 18 November 2013.

Yin, A. (2012), Structural analysis of the Valles Marineris fault zone: Possible evidence for large-scale strike-slip faulting on Mars, *Lithosphere*, *4*(4), 286–330, doi:10.1130/L192.1. [Available at http://lithosphere.geoscienceworld.org/content/4/4/286.full.], Accessed 14 February 2014.

Zurek, R. W., and S. E. Smrekar (2007), An overview of the Mars Reconnaissance Orbiter (MRO) science mission, *J. Geophys. Res.*, *112*, E05S01, doi:10.1029/2006JE002701.

Erratum

In the originally published version of this article, contributing author Sandra M. Wiseman's name was misspelled. In addition, there was an error in row 14 of Table 2 under the "formulation" and "kernel width" columns. The updated equation now reflects the true OLINDEX3 formulation, and the one that is used in products delivered to the PDS. These errors have has since been corrected and this version may be considered the authoritative version of record.